Alma Mater Studiorum · Università di Bologna

Scuola di Scienze
Dipartimento di Fisica e Astronomia
Corso di Laurea in Fisica

X-RAY ABSORPTION FINE STRUCTURE ANALYSIS: DEVELOPMENT OF DATA PROCESSING TOOLS AND EXPERIMENTAL TECHNIQUES

Relatore:
Prof. Federico Boscherini

Correlatore:
Dott. Francesco d'Acapito

Presentata da:
Gabriele Donati

Anno Accademico 2023/2024

Abstract

Nella Linea Italiana di Spettroscopia di Assorbimento (LISA) situata all'interno dell' European Synchrotron Radiation Facility a Grenoble (Francia), vengono eseguiti esperimenti di Spettroscopia di Assorbimento di raggi-X utilizzando la rivelazione in fluorescenza per studiare la struttura atomica o molecolare di numerosi materiali. I metodi attuali di acquisizione dati presentano però una criticità. In particolare, non è consentito memorizzare e post-processare gli spettri di fluorescenza completi una volta terminata l'acquisizione dei dati, e quindi definire un dominio di integrazione dello spettro di fluorescenza diverso da quello specificato a monte. Di conseguenza non è possibile adattare in maniera mirata al campione studiato la regione di interesse per l'estrazione del segnale EXAFS. Nel lavoro a seguire, si cerca di risolvere questa problematica sviluppando un metodo di acquisizione dati in grado di salvare per intero gli spettri di fluorescenza, e un programma in grado di elaborarne il contenuto e correggerli di tempo morto ad acquisizione completata. Dunque, sono state effettuate misure di prova che hanno validato con ottima confidenza la tecnica in questione, evidenziando miglioramenti del segnale EXAFS estratto grazie a questa analisi fatta a posteriori. In particolare, si è evidenziata una notevole riduzione del rapporto segnale-rumore, dovuta alla particolare flessiblità del metodo sviluppato. Infatti, i software di LISA effettuano la correzione del tempo morto durante il processo di acquisizione, aumentando i tempi di misura soprattutto ad alti conteggi. Al contrario, la tecnica sviluppata trova applicazione ad acquisizione completata, aumentando la precisione dei dati raccolti e permettendo di adattare in maniera più efficace le condizioni sperimentali alle specifiche caratteristiche del campione.

Contents

Introduction

Extended X-ray absorption fine structure is the oscillatory variation of the X-ray absorption index as a function of photon energy beyond an absorption edge. An in-depth study of this topic is of paramount importance, especially for the wide range of its applications. Its interests range from physics to chemistry, and it is also essential for seemingly more distant subjects such as molecular biology or medicine. The X-ray absorption index can be readily measured by colliding a beam of monochromatic photons with a sample of low-dilute matter and subsequently evaluating the fluorescence spectrum of the emitted radiation. As a matter of fact, from an experimental standpoint, the absorption is proportional to the ratio between the intensity of the emitted fluorescence radiation, and the intensity just prior to hitting the sample. The choice of absorption edge to be focused on will determine the necessity of performing an energy scan within the energy range that includes the latter's energy. Consequently, for each incoming beam energy we are adequately equipped to asses the fluorescence radiation intensity from the energetic spectrum by summing the counts of the various energetic bins within the specified interest interval (the Region of Interest or ROI). The current experimental methods employed at the LISA Beamline at ESRF do not permit users to isolate the specified interval once the data acquisition process has been completed. In other words, it is imperative that a region of interest be defined prior to acquiring the spectrum. Once this is done, the entire spectrum is deleted, and only the value of the intensity for each energy is retained. Furthermore, given the elevated photon count rates, the likelihood of pile-up inspection is high. Consequently, during data acquisition, it is of paramount importance to correct the total counting for dead time. This is automatically done by the current instrumentation at LISA for each incoming energy step.

Nevertheless, there are instances when it is not feasible to ascertain the width of the region of interest a priori to the acquisition process. This may be due to a lack of comprehensive understanding of the behaviour of the sample subjected to high-energy radiation or to the fact that the determination of this parameter depends on the specifications of the experimental apparatus. The objective of our work is to develop data processing tools that enable users to define at will the region of interest according to their specific requirements, after viewing the entire spectrum. Additionally, it is imperative to develop a revised dead-time correction methodology that aligns with this novel approach and is applicable to all delineations of the region of user-defined integration. Moreover, the new method would yield the same results as the previous method in the limit case where the pre-defined ROI and the user-defined ROI are identical. Actually, it will be demonstrated that a significant enhancement of the signal can be attained.

Introduction to X-Ray Absorption Spectroscopy

X-ray absorption spectroscopy (XAFS) provides pivotal information about the inner atomic or molecular structure of matter. In this first chapter, we will introduce the main mathematical elements necessary for a complete understanding of this phenomenon. The chapter begins with an overview of the interaction between matter and radiation, emphasizing the quantum nature of the electromagnetic field and its behavior when interacting with other particles. Next, we will discuss the quantum atomic structure of matter, focusing on the eigenvalue problem in Schrödinger's equation and the computation of the eigenvalues and eigenstates of a general multi-electronic atom. Finally, we will present the basic theory of XAFS, highlighting the mathematical and phenomenological aspects of this technique.

1.1 Matter and radiation interaction

1.1.1 Quantization of electromagnetic field

Classical electromagnetism [6] is completely contained within Maxwell's equations, which govern the dynamics of the *electric field* $\mathbf{E}(\mathbf{x}, t)$ and the *magnetic field* $\mathbf{B}(\mathbf{x}, t)$. In Gaussian units, Maxwell's equations are as follows:

$$\nabla \cdot \mathbf{E} = 4\pi\rho \tag{1.1}$$

$$\nabla \times \mathbf{B} - \frac{1}{c}\frac{\partial \mathbf{E}}{\partial t} = \frac{4\pi \mathbf{J}}{c} \tag{1.2}$$

$$\nabla \cdot \mathbf{B} = 0 \tag{1.3}$$

$$\nabla \times \mathbf{E} + \frac{1}{c}\frac{\partial \mathbf{B}}{\partial t} = 0 \tag{1.4}$$

where $\rho = \rho(\mathbf{x}, t)$ is the charge density and $\mathbf{J} = \mathbf{J}(\mathbf{x}, t)$ is the current density. From equations (1.3) and (1.4), we can redefine the magnetic and electric fields using the *electromagnetic potentials*, which consist of the *vector potential* $\mathbf{A}(\mathbf{x}, t)$, such that:

$$\mathbf{B} = \nabla \times \mathbf{A}, \tag{1.5}$$

and the *scalar potential* $\varphi(\mathbf{x}, t)$, such that:

$$\mathbf{E} = -\nabla\varphi - \frac{1}{c}\frac{\partial \mathbf{A}}{\partial t} \tag{1.6}$$

The definitions of $\mathbf{A}$ and φ do not uniquely determine the electric and magnetic fields. In particular, the following transformations:

$$\mathbf{A} \to \mathbf{A}' = \mathbf{A} + \nabla\chi \tag{1.7}$$

$$\varphi \to \varphi' = \varphi - \frac{1}{c}\frac{\partial \chi}{\partial t} \tag{1.8}$$

where $\chi = \chi(\mathbf{x}, t)$ is an arbitrary scalar function, do not change the electric and magnetic fields. These transformations, known as *gauge transformations*, leave Maxwell's equations unchanged and reveal a deep symmetry within electromagnetism. It is usual to apply the *Coulomb gauge*, where $\chi(\mathbf{x}, t)$ is chosen to obtain $\varphi = 0$ and $\nabla \cdot \mathbf{A} = 0$.

Another essential property is that all the components of the vector potential satisfy the D'Alembert equation [29]:

$$\nabla^2 \mathbf{A}(\mathbf{x}, t) - \frac{1}{c^2}\frac{\partial^2 \mathbf{A}}{\partial t^2}(\mathbf{x}, t) = 0. \tag{1.9}$$

The above wave equation has plane wave solutions $e^{i\mathbf{k}\cdot\mathbf{x}-\omega_{\mathbf{k}}t}$ at angular frequency $\omega_{\mathbf{k}}$ and wave vector $\mathbf{k}$.
Now suppose that the total field is contained within some volume V. Boundary conditions imposed on a wave in a confined volume require the wave to vanish at the edges, allowing only specific discrete wavevector $\mathbf{k}$. The Fourier expansion over a collection of these modes is therefore:

$$\mathbf{A}(\mathbf{x},t) = \frac{1}{2\sqrt{V}}\sum_{\mathbf{k}}[\mathbf{A}_{\mathbf{k}}(t)e^{i\mathbf{k}\cdot\mathbf{x}} + \mathbf{A}^*_{\mathbf{k}}(t)e^{-i\mathbf{k}\cdot\mathbf{x}}] \tag{1.10}$$

where each coefficient $\mathbf{A}_{\mathbf{k}}(t)$ is an amplitude for a wave at the stated wave vector and the different modes are orthogonal. The time dependence of $\mathbf{A}_{\mathbf{k}}(t)$ is of exponential type and is implicitly contained within it. Furthermore, the gauge assumption $\nabla\cdot\mathbf{A}=0$ translates to $\mathbf{k}\cdot\mathbf{A}_{\mathbf{k}}=0$, which shows that the waves are transverse. Since for any $\mathbf{k}$ there are two transverse directions, there will be two independent polarization directions, identified by unit vectors $\mathbf{e}_{\mathbf{k}\alpha}$, $\alpha=1,2$.

Based on equation (1.10), and by the formal transformation $\nabla\to\pm i\mathbf{k}$, we obtain the electric and magnetic fields from (1.5) and (1.6):

$$\mathbf{E}(\mathbf{x},t) = \frac{i}{2c\sqrt{V}}\sum_{\mathbf{k}}\omega_{\mathbf{k}}[\mathbf{A}_{\mathbf{k}}(t)e^{i\mathbf{k}\cdot\mathbf{x}} - \mathbf{A}^*_{\mathbf{k}}(t)e^{-i\mathbf{k}\cdot\mathbf{x}}] \tag{1.11}$$

$$\mathbf{B}(\mathbf{x},t) = \frac{i}{2\sqrt{V}}\sum_{\mathbf{k}}\mathbf{k}\times[\mathbf{A}_{\mathbf{k}}(t)e^{i\mathbf{k}\cdot\mathbf{x}} - \mathbf{A}^*_{\mathbf{k}}(t)e^{-i\mathbf{k}\cdot\mathbf{x}}] \tag{1.12}$$

From these equations, it is straightforward to calculate the net total energy:

$$H = \frac{1}{8\pi}\int_V d^3\mathbf{x}(|\mathbf{E}|^2+|\mathbf{B}|^2) = \frac{1}{8\pi}\sum_{\mathbf{k}}k^2|\mathbf{A}_{\mathbf{k}}|^2 = \frac{1}{4\pi}\sum_{\mathbf{k},\alpha}k^2|\mathbf{A}_{\mathbf{k}\alpha}|^2. \tag{1.13}$$

This Hamiltonian shows that the modes do not interfere with each other.

It is particularly interesting to transform this Hamiltonian into the language of coordinates and conjugate momenta. The canonical momentum $\mathbf{p}$ is defined as:

$$\mathbf{p} = -\frac{1}{4\pi c}\mathbf{E} = -\frac{i}{8\pi c^2\sqrt{V}}\sum_{\mathbf{k}}\omega_{\mathbf{k}}[\mathbf{A}_{\mathbf{k}}(t)e^{i\mathbf{k}\cdot\mathbf{r}} - \mathbf{A}^*_{\mathbf{k}}(t)e^{-i\mathbf{k}\cdot\mathbf{r}}]. \tag{1.14}$$

This suggests the introduction of the momenta at each wave vector:

$$\mathbf{P}_{\mathbf{k}}(t) = -\frac{i\omega_{\mathbf{k}}}{4\pi c^2}\mathbf{A}_{\mathbf{k}}(t). \tag{1.15}$$

The generalized coordinates are the components of $\mathbf{A}$:

$$\mathbf{q}_{\mathbf{k}} = \mathbf{A}_{\mathbf{k}}. \tag{1.16}$$

Hence, the total canonical Hamiltonian, expressed in the Fourier modes, looks like:

$$H = 2\pi c^2 \sum_{\mathbf{k}} \mathbf{p}_{\mathbf{k}} \cdot \mathbf{p}^*_{\mathbf{k}} + \frac{1}{8\pi c^2} \sum_{\mathbf{k}} \omega^2_{\mathbf{k}} \mathbf{q}_{\mathbf{k}} \cdot \mathbf{q}^*_{\mathbf{k}}. \tag{1.17}$$

From the already demonstrated mode independence, it is evident that there is a tight analogy between the individual mode and the harmonic oscillator Hamiltonian, which we remember to be:

$$H = \frac{p^2}{2m} + \frac{m\omega^2}{2} q^2. \tag{1.18}$$

Formally following the quantization of the harmonic oscillator, let's introduce the annihilation and creation operator pair for both the positive and negative wave vectors:

$$a_{\mathbf{k}} = \frac{1}{\sqrt{2}}(Q_{\mathbf{k}} + iP_{\mathbf{k}}), \quad a^\dagger_{\mathbf{k}} = \frac{1}{\sqrt{2}}(Q^\dagger_{\mathbf{k}} - iP^\dagger_{\mathbf{k}}), \tag{1.19}$$

$$a_{-\mathbf{k}} = \frac{1}{\sqrt{2}}(Q^\dagger_{\mathbf{k}} + iP^\dagger_{\mathbf{k}}), \quad a^\dagger_{-\mathbf{k}} = \frac{1}{\sqrt{2}}(Q_{\mathbf{k}} - iP_{\mathbf{k}}). \tag{1.20}$$

where $P_{\mathbf{k}}$ and $Q_{\mathbf{k}}$ are the rescaled coordinates and momenta, defined as:

$$P_{\mathbf{k}} = \sqrt{\frac{4\pi c^2}{\hbar\omega_{\mathbf{k}}}} p_{\mathbf{k}}, \quad Q_{\mathbf{k}} = \sqrt{\frac{\omega_{\mathbf{k}}}{4\pi\hbar c^2}} q_{\mathbf{k}}, \tag{1.21}$$

and satisfy the commutation relationship $[a_{\pm\mathbf{k}}, a^\dagger_{\pm\mathbf{k}}] = 1$.
Using these operators, we can rewrite the total Hamiltonian as:

$$H = \sum_{\mathbf{k},\alpha} \hbar\omega_{\mathbf{k}\alpha}(n_{\mathbf{k}\alpha} + \frac{1}{2}), \tag{1.22}$$

where $n_{\mathbf{k}\alpha}$ is called the number operator and is defined as $n_{\mathbf{k}\alpha} = a^\dagger_{\mathbf{k}} a_{\mathbf{k}}$. Thus, the operator $n_{\mathbf{k}\alpha}$ constitute a Heisemberg set of H. Let $|n_{\mathbf{k}\alpha}\rangle$ be an orthonormal basis of eigenkets of the number operator. Then the state $|\psi_{\mathbf{k},\alpha}\rangle$ is a superposition of eigenstates of the number operator:

$$|\psi_{\mathbf{k},\alpha}\rangle = \sum_{n_{\mathbf{k}\alpha}} c_{n_{\mathbf{k}\alpha}} |n_{\mathbf{k}\alpha}\rangle \tag{1.23}$$

We conclude that each mode specified by a wave vector is equivalent, mathematically, to a simple harmonic oscillator, and the modes are completely independent. There is just a linear superposition of their electromagnetic fields. These fields are determined by inserting the quantized vector potential:

$$\mathbf{A}(\mathbf{x}, t) = \sqrt{\frac{2\pi c^2\hbar}{V}} \sum_{\mathbf{k},\alpha} \frac{\mathbf{e}_{\mathbf{k}\alpha}}{\sqrt{\omega_{\mathbf{k}}}} [a_{\mathbf{k}\alpha} e^{i\mathbf{k}\cdot\mathbf{x}} + a^\dagger_{\mathbf{k}\alpha} e^{-i\mathbf{k}\cdot\mathbf{x}}] \tag{1.24}$$

into equations (1.11) and (1.12).

1.1.2 Atoms, molecules and radiations

Now we are up to the task of studying matter-radiation interaction. In particular, since we are interested in atomic or molecular interactions, a nonrelativistic treatment is sufficient. The state of a molecule is encoded in a normalized ket $|\psi\rangle$, defined up to a phase factor, in a Hilbert space that satisfies the Schrödinger equation:

$$i\hbar\frac{d}{dt}|\psi(t)\rangle = H|\psi(t)\rangle \tag{1.25}$$

In the Schrödinger representation, the wavefunction depends on the coordinates ($\mathbf{x}$) of all the particles constituting the matter, i.e. of the electrons and of the nuclei, and is defined as $\psi(\mathbf{x},t) = \langle\mathbf{x}|\psi(t)\rangle$. To simplify the problem and find solutions that describe the system, several approximations are necessary. Firstly, the *Born-Oppenheimer approximation* assumes that the nuclei are stationary at their equilibrium positions. The second approximation is the *mean field approximation*, which averages out electron correlation effects, allowing electrons to move in a mean field generated by other electrons. The third approximation is the *one electron approximation*, which isolates the wavefunction of a specific electron from the rest of the total wavefunction. By the one electron approximation, we consider a single particle of charge q as it interacts with the field. To avoid overly complicated calculations, let's consider the interaction between a hydrogen-like atom and an electromagnetic wave. This example is very important because it describes the situation more easily, while also highlighting the main characteristics. This simplification helps us focus on fundamental quantum mechanical principles without the additional complexities of multi-electron systems.

A hydrogen-like atom is a system consisting of a nucleus with charge $+Ze$ (where Z is the atomic number and e is the elementary charge) and a single electron. The Hamiltonian of the unperturbed particle has the form:

$$H_0 = \frac{\mathbf{p}^2}{2m} - \frac{Ze^2}{r} \tag{1.26}$$

And form a complete system of commuting self-adjoint operators with the square l^2 and the component l_0 of the angular momentum operator l. From the quantum theory, it follows that must exist an orthonormal basis $|n,l,m_l\rangle$ of simultaneous eigenkets of H_0, l^2 and l_0, where n,l,m_l are integer with n positive, $l = 0,1,2,...$ and $m_l = -l, -l+1, ..., l-1, l$. The eigenvalues relation reads as:

$$\begin{aligned} H|n,l,m_l\rangle &= |n,l,m_l\rangle\, w_n, \\ l^2|n,l,m_l\rangle &= |n,l,m_l\rangle\, \hbar^2 l(l+1), \\ l_0|n,l,m_l\rangle &= |n,l,m_l\rangle\, \hbar m_l \end{aligned} \tag{1.27}$$

Where $w_n = -(Z^2e^2)/(2r_B n^2)$ is the discrete hydrogen-like energy spectrum. We are interested in studying the transition probability of an hydrogen-like atom after a time-dependent perturbation. In particular, as previously deduced, the perturbation induced by an electromagnetic wave has a harmonic time-dependence, so we are allowed to model

the process with perturbation theory using a periodic perturbation. We can describe the dynamic of the system with the complete Hamiltonian:

$$H(t) = H_0 + H'(t) \tag{1.28}$$

where $H'(t)$ is the perturbation of the system. Specifically, we are able to compute the transition probability of the electron between two imperturbed states produced by a harmonic electromagnetic Hamilonian $H'(t)$:

$$H'(t) = -\frac{e}{mc}\mathbf{p} \cdot \mathbf{A(x,t)} \tag{1.29}$$

Here we have neglected the terms of second order in $\mathbf{A}$.

As the latter is a periodic function of time, it has an expansion in Fourier series:

$$H'(t) = \sum_n \exp(-i\omega_n t) H'_n \tag{1.30}$$

Where the ω_n are the distinct proper frequencies of $H'(t)$ and H'_n is time independent. As $H'(t)$ represents an observable, it has to be self-adjoint, so $H(t)' = H'(t)^\dagger$, for each time t, so:

$$H'(t) = \sum_{n>0} \exp(-i\omega_n t) H'_n + H'_0 + \sum_{n>0} \exp(i\omega_n t) H'^\dagger_n \tag{1.31}$$

Let $|n, l, m_l\rangle$ the state in which the system is prepared in at the initial time s, the probability $P(n, l, m_l \to n', l', m'_l; t, s)$ that the system is found in the state $|n', l', m'_l\rangle$ at the time t is a periodic function of both t and s. A more meaningful object to study in this case is the transition probability rate $W(n, l, m_l \to n', l', m'_l)$, that expresses the time averaged fraction of the systems prepared in the state initial in the remote past which undergo the transition to the final state per unit time. It turns out that this latter physical quantity is independent from t. For $n' \neq n$, $l' \neq l$ and $m'_l \neq m_l$, to lowest non trivial order in perturbation theory, one has then:

$$W(n, l, m_l \to n', l', m'_l) \simeq \frac{2\pi}{\hbar^2} \sum_n |\left\langle n', l', m'_l \right| H'_n \left| n, l, m_l \right\rangle|^2 \delta(w_{n'} - w_n - \hbar\omega_n) \tag{1.32}$$

Hence, in the simplified case where the electromagnetic field could be approximate as monochromatic, the transition probability is significantly different from zero only when the energy difference between the two states equals the photon's energy. That means that two different phenomena could occur in this situation. [1]

Stimulated absorption occurs when a photon of energy $\hbar\omega$ is absorbed by the atom, causing the electron to transition from the state labeled by n to n' where $n' > n$. Conversely, *stimulated emission* occurs when a photon is emitted simultaneously with a transition from n to n' where $n > n'$.

[1] The presence of the delta function makes the situation appear unphysical: the probability is always 0 except at resonance where it diverges. Actually it emerges from the following relation: $\lim_{\eta\to 0^+} \frac{1}{\pi} \frac{\eta}{\omega^2+\eta^2} = \delta(\omega)$ during the computation of 1.32. See Figure 1.1

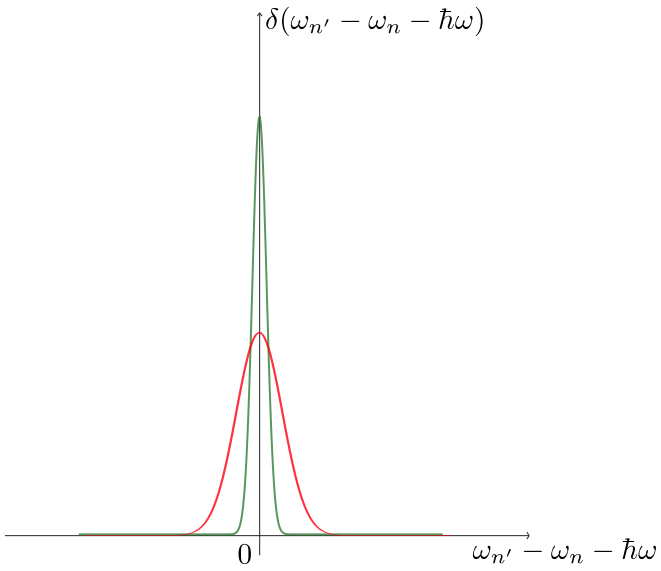

Figure 1.1: *The curves δ the delta function as $\eta \to 0^+$. Above, we plot $\delta(\omega)$ for $\eta = 1, 1/2$ (red, green)*

Let's focus for a while on the stimulated absorption, supposing that the incident electromagnetic wave is monochromatic (of frequency ω) and has a linear polarization. So, the eq. 1.32 reads:

$$W(n,l,m_l \to n',l',m_l') \simeq \frac{4\pi^2 e^2 \hbar}{mV\omega} a_{\mathbf{k}}^2 \left|\langle n',l',m_l'| \exp(i\mathbf{k}\cdot\mathbf{x})\mathbf{e}_{\mathbf{k}}\cdot\nabla |n,l,m_l\rangle\right|^2 \times \delta(\omega_{n'} - \omega_n - \hbar\omega)$$

This transition probability rate simplifies when the radiation involved is low-energy, such as ultraviolet (UV) radiation or visible light. Specifically, for weak electromagnetic radiation, the wavelength is much larger than the spatial extent of the initial state's wave function. In this case, the wave vector $\mathbf{k}$ of the radiation is approximately $\sim 10^5$ cm^{-1}, allowing us to apply the *dipole approximation*:

$$\exp(i\mathbf{k}\cdot\mathbf{x}) = 1 \tag{1.33}$$

By virtue of this approximation, we find that the transition probability rate assumes the simplified version:

$$W(n,l,m_l \to n',l',m_l') \simeq \frac{\pi\omega e^2}{\varepsilon_0 V} \left|\langle n',l',m_l'| \mathbf{e}_{\mathbf{k}}\cdot\nabla |n,l,m_l\rangle\right|^2 \times \delta(w_{n'} - w_n - \hbar\omega)$$

This approximation is not valid for X-ray radiation interacting with valence electrons, as their spatial extent is too large compared to the wavelength of the radiation. However, it

is applicable to interactions with deep core electrons, which have a significantly smaller spatial extent. Consequently, for core electrons, the dipole approximation can be used effectively.

In the case where the electromagnetic field involved is weak, it is possible to study these interaction phenomena as a scattering experiment, where a beam of identical particles (photons) interacts with a sample of identical scatterers (the external electrons). The number $\Delta N(n,l,m_l \rightarrow n',l',m_l')$ of systems undergoing a state transitions $n,l,m_l \rightarrow n',l',m_l'$ occurring in the time interval Δt will be proportional to the number current density J of the photons and the number N_{n,l,m_l} of the scatteres in the initial state n,l,m_l an to Δt. Hence, we have:

$$\Delta N(n,l,m_l \rightarrow n',l',m_l') = JN_{n,l,m_l}\Delta t\sigma(n',l',m_l' \leftarrow n,l,m_l) \tag{1.34}$$

Here, the coefficient of proportionality $\sigma(n,l,m_l \rightarrow n',l',m_l')$ is the *differential cross section* for the transition $n,l,m_l \rightarrow n',l',m_l'$. $\sigma(n,l,m_l \rightarrow n',l',m_l')$ has the dimension of a length squared. According to quantum theory, the differential cross section for the transition $n,l,m_l \rightarrow n',l',m_l'$, with $n \neq n'$, $l \neq l'$ and $m_l \neq m_l'$ reads:

$$\sigma(n,l,m_l \rightarrow n',l',m_l') \simeq \frac{2\pi}{\hbar^2 J}\sum_{n>0} |\left\langle n',l'm_l'\right| H_n' \left|n,l,m_l\right\rangle|^2 \delta(w_{n'} - w_n - \hbar\omega_n) \tag{1.35}$$

This relation is called *Fermi's golden rule.*

1.2 The atomic structure

Having discussed the interaction of radiation with matter, we can now delve into the atomic structure of multi-electron atoms, starting from the solution of the Schrödinger equation 1.25. This foundation will provide a profound understanding of spectroscopy, enabling us to interpret the experimental results that will be presented later.

A multi-electron atom of atomic number Z contains a nucleus of charge $+Ze$ surrounded by Z electrons each of charge $-e$. Each electron is affected by the presence of an attractive Coulomb field, due to the nucleus, and of a repulsive Coulomb field exerted by all the other $Z-1$ electrons. Therefore, the total Hamiltonian of the system will be:

$$H = -\sum_{i=1}^{Z}\left[\frac{\hbar^2}{2m}\nabla_i^2 + \frac{Ze^2}{x_i}\right] + \sum_{i=1}^{Z}\sum_{j>i}^{Z}\frac{e^2}{|\mathbf{x}_i - \mathbf{x}_j|} \tag{1.36}$$

Solving this problem as given is practically impossible due to the complexity arising from the interactions terms. Indeed, the exact solution of the Schrödinger equation for such a system is not feasible because the electron-electron repulsion terms introduce significant mathematical difficulties. Consequently, some approximations are necessary to make the problem tractable. In a typical multi-electron atom, there are so many interaction between an electron and all the other electrons that their net effect is very strong except if the electron is quite near the nucleus (Fig. 1.2). Just as molecules within a water droplet experience stronger interactions with other molecules when they are on the surface, electrons closest to the nucleus tend to be less affected by the presence of other electrons because the sum of the forces balances out. This analogy helps to explain the concept of electron shielding in multi-electron atoms.

Figure 1.2: *Left: The nucleus exerts a strong attractive force on an electron near the atom's surface, while the other electrons apply weak repulsive forces. The net impact of these repulsive forces is significant. Right: The nucleus exerts a very strong attractive force on an electron close to the atom's center, while the other electrons apply weak repulsive forces. (The figure was redrawn: it is based on Fig. 9-8 of [9])*

Inner electrons are more tightly bound to the nucleus, and the forces from other electrons tend to counterbalance, reducing the net repulsive effect. In contrast, outer electrons are more exposed to these repulsive interactions because they are farther from the nucleus and less shielded. Hence, we are led to think that each electron experiences the net potential differently depending on how far it is from the nucleus. In practice, this requirement means that the motion of one electron does not depend on the motion of the others, and so hat the atomic electrons must be treated as moving independently. Then the time-independent Schrödinger equation (1.36) can be separated into a set of equations, one for each electron. Furthermore each electron could be considered as moving in a spherically symmetrical *net potential* $V(r)$, where r is the radial coordinate of the electron with respect to the nucleus. The net potential is the sum of the spherically symmetrical attractive Coulomb potential due to the nucleus and a spherically symmetrical repulsive potential which represents the average effect of the repulsive Coulomb interaction between a typical electron and its $Z-1$ colleagues. As a consequence, the total electric potential exhibits this asymptotic behavior:

$$V(x) = \begin{cases} -\dfrac{Ze^2}{|x|} \text{ if } |x| \to 0 \\ -\dfrac{e^2}{|x|} \text{ if } |x| \to \infty \end{cases} \tag{1.37}$$

Finding the net potential of an atom at distances between its nucleus and outer electron shells may seem daunting, as it hinges on the intricate arrangement of the electron charges. However, we can resolve this by ensuring the net potential is internally coherent or *self-consistent*. This means that when we calculate the distribution of electron charges based on the correct net potential, and then reevaluate the net potential using this charge distribution, the resulting potential must match what we started with. This requirement uniquely determines the accurate net potential for the atom. In spherical coordinates the i-th equation will be:

$$-\frac{\hbar^2}{2m}\nabla^2\psi(r,\theta,\varphi) + V(r) = E\psi(r,\theta,\varphi) \tag{1.38}$$

From quantum theory, considering that the potential depends solely on the radial coordinate, the solution to the former differential equation can be expressed as follows:

$$\psi_{n,l,m_l,m_s}(r,\theta,\varphi) = \frac{R_{n,l}(r)}{r} Y_{l,m_l}(\theta,\varphi)\chi_{m_s} \tag{1.39}$$

where n, l, m_l, and m_s vary, with l and m_l being integers satisfying $l \geq 0$ and $|m_l| \leq l$. The integers l and m_l are known as the *orbital* and *magnetic quantum numbers* respectively. The function R depends solely on the shape of the potential $V(r)$. χ_{m_s} represents the spin eigenfunction and depends on a semi-integer *spin quantum number*. Additionally, employing the Condon-Shortley phase convention, the spherical harmonics $Y_{l,m_l}(\theta,\varphi)$ are defined as:

$$Y_{l,m_l}(\theta,\varphi) = (-1)^{m_l}\left[\frac{2l+1}{4\pi}\frac{(l-m_l)!}{(l+m_l)!}\right]^{1/2} P_l^{m_l}(\cos\theta)\exp(im_l\varphi) \tag{1.40}$$

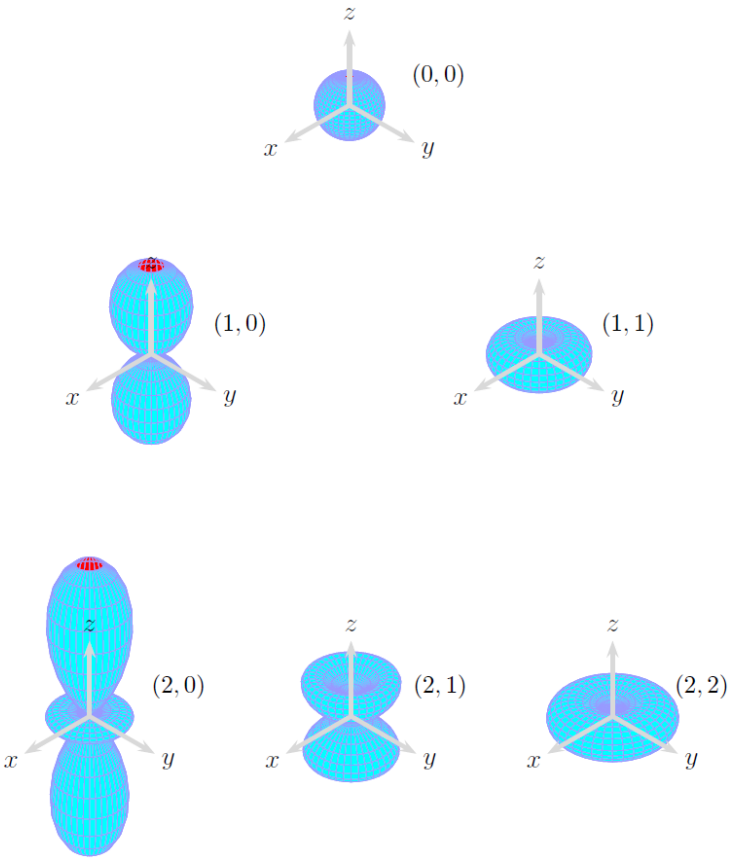

Figure 1.3: *Visualization of the spherical harmonics* $Y_{lm}(\theta, \phi)$ *by plotting the functions* $|Y_{lm}|^2$ *for the first few* l *and* m *values. The distance of the intersection of the direction line specified by the spherical angles* θ *and* ϕ *with the surface of the plot from the origin is proportional to* $|Y_{lm}(\theta, \phi)|^2$*. (The figure is the* 4.13.4 *of [31])*

where $P_l^{m_l}(x)$ denotes the Legendre functions. These functions are crucial as they describe the angular shape of the wavefunction (see Figure 1.3), independent of the potential.

Conversely, the radial dependence of the eigenfunctions for an electron in a multi-electron atom is not known a priori; it depends on the potential. The complete solution of Equation 1.38 can be obtained numerically. The radial probability densities $\rho_{n,l} = |R_{n,l}|^2$ are relevant in atomic physics: $dr\rho_{n,l}(r)$ is the probability of finding the electron at a distance in the range between r and $r + dr$ from the force center. Another crucial result obtained from solving the time-independent Schrödinger equation is the binding energy of each electron in an atom, enabling us to determine the energy levels of any multi-electron atom. The guiding principle in studying the energetic properties of atoms is Pauli's exclusion principle, which in this context manifests as follows: In a multi-electron atom, electrons fill available energy levels in such a way as to achieve the lowest-energy configuration, while maintaining an anti-symmetric wavefunction. This behavior leads to

the arrangement of electrons in atomic orbitals according to the Aufbau principle, whereby electrons occupy the lowest available energy levels before filling higher ones. The following *spectroscopy notation* is commonly used in discussing the spectra and energy levels of the electrons.

l	1	2	3	4	5	6	7	8	9
spectroscopy	s	p	d	f	g	h	i	l	m

The number before the letter indicates the energy level of the orbital. For example, a nl orbital is at the n energy level and is of the l type. Given that the behavior of an atom at this level of approximation depends only on the behavior of electrons, we can fully characterize it by specifying the quantum numbers n and l of all electrons. We refer to the arrangement of occupied electron shells by all electrons as the *configuration* of the atom.

Figure 1.4 shows how the energy of the first energy levels in a multi-electron atom varies with Z. We should not be surprised to find some energy levels with higher principal quantum numbers at lower energies compared to those with lower principal quantum numbers

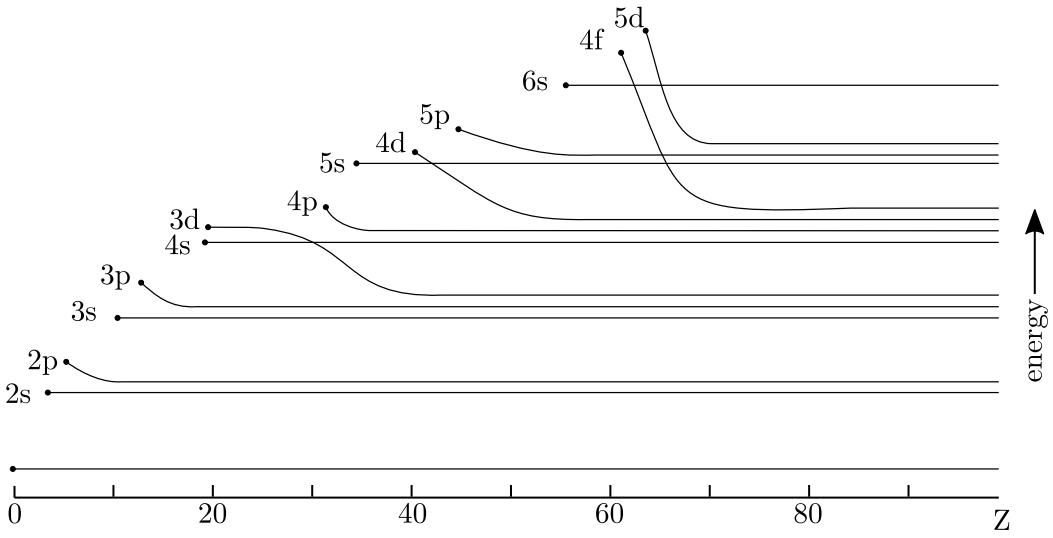

Figure 1.4: *A schematic representation of the energy ordering of all the subshell atom, as a function of its atomic number Z.*(The figure was redrawn: it is based on Fig. 9-14 of [9])

1.3 Basic XAFS theory

After examining the fundamental theoretical aspects of the radiation-matter interaction, we now have the necessary tools to understand this dynamic through experimental observation.

1.3.1 The linear attenuation coefficient

When a collimated X-ray beam passes through a volume, it loses intensity due to two processes: *photoelectric absorption* and *scattering*. The first process was discussed in detail in Section 1.1.2, and can be summarized as follows: a photon is absorbed from the beam, resulting in the ionization or excitation of an atom. The second process involves the deflection of a photon's trajectory due to its collision with an electron.

The main physical parameter describing this phenomenon is the *linear attenuation coefficient* μ. This parameter satisfies the differential equation:

$$\mu = -\frac{1}{\phi}\frac{d\phi}{dz} \tag{1.41}$$

where the flux ϕ is the number of photons per unit time and unit cross-section. Therefore, the linear attenuation coefficient characterizes how easily a volume of material can be penetrated by a radiation. Let us consider a beam prepared in a state n that collides with a matter volume of thickness x. Let ϕ_0 be the flux immediately before colliding with the volume. Then, by equation 1.41, the reduced flux immediately after passing through the volume will be:

$$\phi(x) = \phi_0 \exp(-\mu x) \tag{1.42}$$

It has been experimentally observed that the attenuation coefficient depends on the energy $\hbar\omega$ of the X-ray photons, as well as the composition and density of the sample. Specifically, as the energy increases, the absorption coefficient generally decreases. However, this smooth trend is interrupted by sharp discontinuities known as absorption edges. These occur when the photons have sufficient energy to eject an electron from a deeper atomic level. We shall distinguish several types of edge, depending on the depth of the electron's transition. By standard spectroscopy notation, the highest energy absorption edge, the K edges, correspond to the extraction of an electron from the 1s level. The following table shows the different absorption edges and the corresponding core levels:

Edge	M_V	M_{IV}	M_{III}	M_{II}	M_I	L_{III}	L_{II}	L_I	K
Core level	$3d_{\frac{5}{2}}$	$3d_{\frac{3}{2}}$	$3p_{\frac{3}{2}}$	$3p_{\frac{1}{2}}$	$3s$	$2p_{\frac{3}{2}}$	$2p_{\frac{1}{2}}$	$2s$	$1s$

Because electron binding energies typically increase in a consistent manner with atomic number, each edge energy corresponds to a specific atomic species. Following the absorption of a photon, an isolated atom can undergo two primary outcomes. If the photon's energy matches the energy difference between an electronic core level and an unoccupied bound level, the atom becomes excited. Conversely, if the photon's energy exceeds the

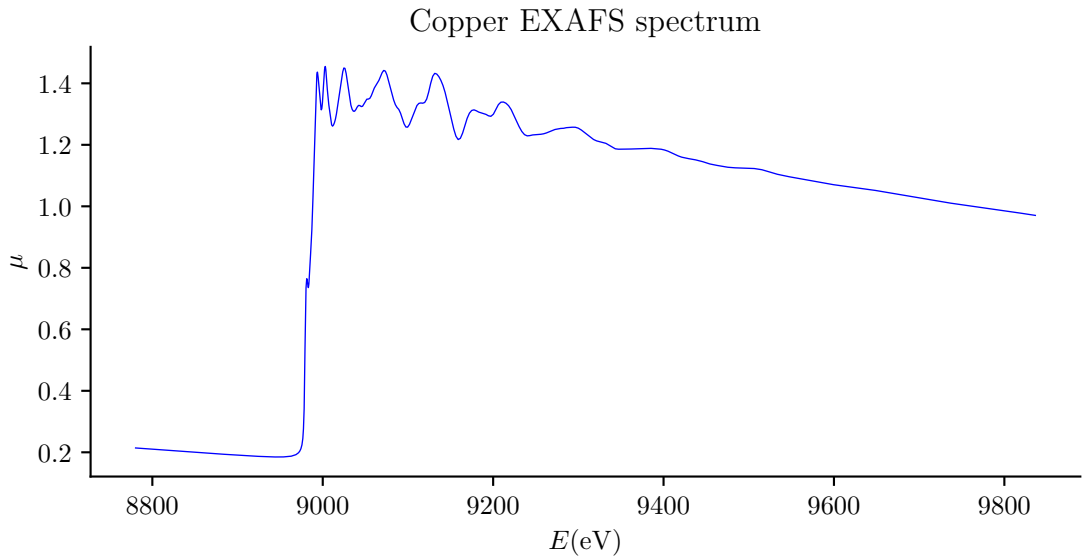

Figure 1.5: *X-ray absorption spectrum of copper at a temperature of* $\sim 100\,\mathrm{K}$. *The sharp rise in* μ *near* $11\,\mathrm{keV}$ *is the* K *edge and the modulation in* μ *above the edge is the EXAFS. This spectrum is sourced from the LISA database[22]*

binding energy, the electron is ejected from the atom, leading to ionization. In the vicinity of an absorption edge, the absorption coefficient reveals a phenomenon known as the *X-ray Absorption Fine Structure* (XAFS). This phenomenon can be divided into three distinct regions, as illustrated in Figure 1.5. The first two regions are the *pre-edge* and *edge*, which are confined to a narrow range of energy, typically just a few electron volts (eV) surrounding the edge. Next, we have the *X-ray Absorption Near Edge Structure* (XANES), encompassing energies approximately $30 - 50eV$ above the edge. Finally, there is the *Extended X-ray Absorption Fine Structure* (EXAFS), extending beyond the XANES region and often spanning up to around one thousand eV for condensed matter samples. We are particularly interested in the study of this latter, and in particular in the quantitative analysis of the oscillations of the x-ray absorption coefficient on the high-energy side of an absorption edge. From an experimental point of view, the K-edge of the main metallic elements is set at the following energies [25]:

Element	K-edge (keV)
Iron (Fe)	7.112
Copper (Cu)	8.978
Zinc (Zn)	9.658
Titanium (Ti)	4.966
Chromium (Cr)	5.989

1.3.2 EXAFS: Theoretical background

When an atom absorbs a high-energy X-ray photon, a core electron, confined to a small orbital within the atom, is ejected and the kinetic energy of this ejected photoelectron is the difference between the photon energy $\hbar\omega$ and the core binding energy E_b. The wavelength λ of the outgoing photoelectron's wavefunction decreases as the photon energy $\hbar\omega$ increases.

The absorption coefficient $\mu(k)$ of the atom, when isolated, is determined by a combination of the localized core wavefunction and the outgoing wavefunction of the photoelectron. However, if the atom is not isolated, the photoelectron can be scattered by neighboring atoms. This introduces an incoming wavefunction into the total photoelectron wavefunction, which becomes a superposition of the outgoing and scattered waves.

The phase relationship between the outgoing and scattered waves, evaluated at the core site of the absorbing atom, depends on the wavelength of the photoelectron and the distance R between the absorbing and scattering atoms. Changes in this phase relationship with varying photon energy $\hbar\omega$ result in a modulation of the absorption coefficient.

The frequency of the oscillations in the Extended X-ray Absorption Fine Structure (EXAFS) depends on the distance between the absorbing and back-scattering atoms, while the amplitude of these oscillations is proportional to the number of back-scattering atoms. The mathematical model that describes what was just said is summarized in the following equation [10]:

$$\chi(k) = \frac{\Delta\mu}{\mu_0} = -\sum_j \frac{N_j}{kr_j^2} |f_j(k,\pi)| \times \sin\left(2kr_j + \psi_j(k)\right) \exp\left\{-2\sigma_j^2 k^2 - \frac{2r_j}{\lambda_j(k)}\right\} \quad (1.43)$$

Where $\chi(k)$, the *EXAFS function*, is the oscillatory part of the absorption coefficient, normalized to the structureless (atomlike) background. Equation 1.43 describes the modification of the photoelectron wave function at the origin due to scattering by N_j neighbors located at a radial distance r_j away. This is illustrated in figure 1.6 where the outgoing wave is shown backscattered by neighboring atom. The backscattering amplitude is given by:

$$f(k,\pi) = \frac{1}{2ik}\sum_l (2l+1)\left(\exp(2i\delta_l) - 1\right)(-1)^l \quad (1.44)$$

where $\delta_l(k)$ are the scattering phase shifts. The photoelectron wave vector k is defined as:

$$k = \hbar^{-1}[2m(\hbar\omega - E_0)]^{1/2} \quad (1.45)$$

It is evident that the electron wave will undergo a shift of $2kr_j$ by the time it completes its trip to the neighboring location. Hence, we must add the total phase function $\psi_j(k)$ given by

$$\psi_j(k) = \phi_j(k) + 2\delta_1'(k) \quad (1.46)$$

The first term represents the phase shift resulting from backscattering off the j-th neighboring atom, as defined in Eq. 1.44. The second term accounts for twice the phase shift of the central atom, reflecting the potential encountered by the $l = 1$ photoelectron wave

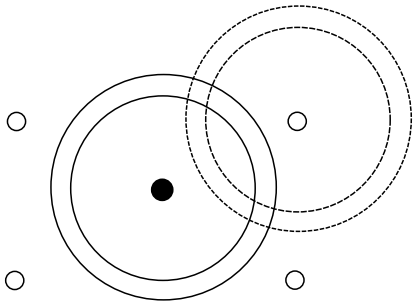

Figure 1.6: *Photoelectron waves emitted outward (solid lines) propagate towards neighboring atoms depicted as open circles. The waves that scatter back (dashed lines) alter the wave function at the central atom and result in EXAFS oscillations. This picture is a remade version of Figure 2 of [10]*

(excited from an $l = 0$ state). The wave function at the origin is modulated by this combined phase factor.

The primary significance of equation 1.43 lies in its potential to invert the problem and determine the distance r_j through analysis of experimental data. Specifically, it has been demonstrated that performing a Fourier transformation in k-space of the EXAFS reveals peaks that correspond to different atomic shells. In this way, we can determine the specific local structure of each atomic species involved in the experiment.

In a simplified model, the photoelectric absorption coefficient is believed to follow the *Victoreen law*, which for an hydrogenlike atom reads:

$$\mu \propto C\lambda^{7/2} \tag{1.47}$$

this proportionality constant, denoted as C, varies with the atomic number Z. However, it's evident that this simplistic approximation falls short of meeting our requirements. Calling attention to previous section, let's suppose that an atom is initially in its ground state $|\psi_i\rangle$ of energy E_i. When it interacts with the electromagnetic field, it has the capability to absorb an X-ray photon with energy $\hbar\omega$ and undergo a transition to a final state $|\psi_f\rangle$ with energy $E_f = E_i + \hbar\omega$. This photon energy can be utilized to elevate an electron from a core level to an unoccupied outer level or to the continuum of free states. It's important to consider ionization to adequately describe *EXAFS*. The absorption coefficient can be expressed as:

$$\mu(\omega) = n\sigma(\hbar\omega) \propto n \sum_f W(i \to f) \tag{1.48}$$

Where n is the number of atoms per unit volume, σ is the atomic absorption cross section and $W(i \to f)$ is the transition rate summed over all the electrons inside the atom:

$$W(i \to f) = \frac{1}{c}\left(\frac{2\pi e}{m\hbar\omega}\right)^2 I_\alpha(\omega) |\langle\psi_f| \sum_j \mathbf{e_{k\alpha}} \cdot \mathbf{p_j} |\psi_i\rangle|^2 \tag{1.49}$$

Where we had used the dipole approximation 1.33

1.3.3 One electron approximation

In order to gain an understanding of the fundamental principles involved, it is helpful to consider a relatively simple case. In particular, we will demonstrate how the scattering of the primary photoelectron by neighbouring atoms can result in the emergence of the fine structure. To illustrate this, we will examine a two-atom system, comprising an absorber (A) and a scatterer (B), as illustrated in Figure 1.7. Further approximations are made on the basis of considering only one active core electron involved in the photoelectric absorption process, and of disregarding thermal vibrations as insignificant. Furthermore, the effect of multiple scattering by neighbouring atoms is neglected, and the photoelectron scattered by atom B is assumed to be a plane wave.

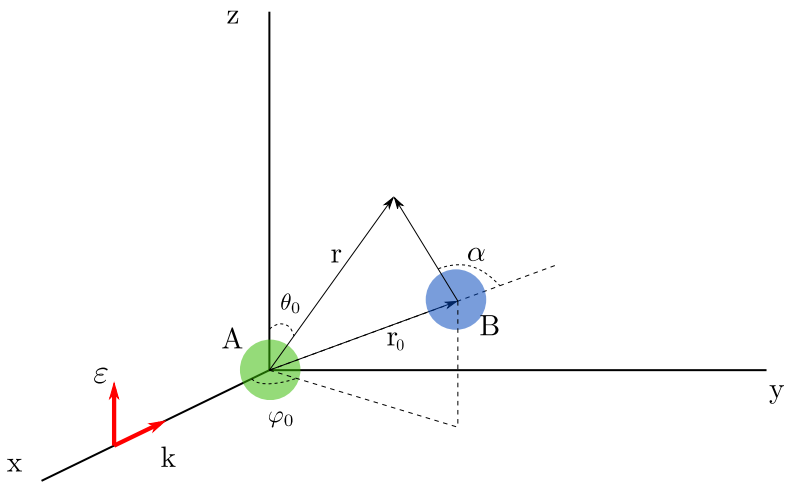

Figure 1.7: *Two-atom system and incident radiation*

In accordance with the Fermi golden rule (equation 1.35), the cross-section for an electron transition between an initial discrete bound state (state i) and a final continuum state f is given by:

$$\sigma(i \to f) = 4\pi^2 \alpha \hbar\omega \left|\langle \psi_i | \boldsymbol{e_k} \cdot \mathbf{r} | \psi_f \rangle\right|^2 \rho(E_f) \tag{1.50}$$

with $\hbar\omega = E_f - E_i$ and the structure constant α. In order to circumvent the necessity of working with challenging atomic potential functions, it is recommended that the space surrounding the two-elements system be divided into three distinct regions, as illustrated in figure 1.8. This approximation, which is commonly referred to as the *Muffin Tin approximation*, entails averaging the potential of the various involved atoms within spherical regions. The first region, designated as region I, represents the spherically averaged potential of the excited atom A. The second region, designated as region II, represents the constant interstitial potential. The third region, designated as region III, represents the

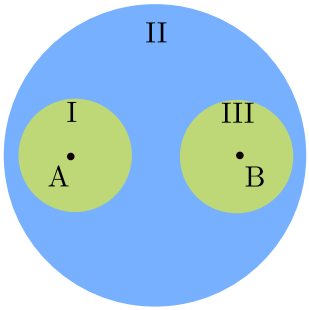

Figure 1.8: *Representation of Muffin Tin approximation*

spherically averaged potential of the scattering atom B. The calculation of the EXAFS function (equation 1.43) is a relatively straightforward process when using this model, as it involves the calculation of the wavefunction of the electron in the specified potential regions. The trajectory of the photoelectron begins with its emission in the direction **k** as a result of the interaction between the incident beam and the atom. At this stage, the wavefunction can be determined by solving the Schrödinger equation with a constant spherical potential. Quantum theory allows for the analytical solution of such equations, with the resulting wavefunction being proportional to the solutions of the Bessel equations.

$$\psi_I(\mathbf{r}) = Y_{1,0}(\theta, \varphi) j_1(kr) \tag{1.51}$$

For the same reasons, in the region II, we can compute the wavefunction of the photoelectron, and it is as follow:

$$\psi_{II}(\mathbf{r}) = \sqrt{\frac{3}{4\pi}} \cos\theta \frac{i}{kr} \exp\big(2i\delta_1'(k)\big) \exp(ikr) \tag{1.52}$$

Then we can compute the back scattered function:

$$\psi_{SC}(\mathbf{r}) = \psi_{II}(\mathbf{r}_0) f(k, \alpha) \frac{\exp(ik|\mathbf{r} - \mathbf{r}_0|)}{|\mathbf{r} - \mathbf{r}_0|} \tag{1.53}$$

and seek which part of this wavefunction has the same angular dependence and the same limit for $r \to 0$ as $\psi_I(\mathbf{r})$, in order to evaluate the final state of the wave function in region I. It is possible to demonstrate that:

$$\psi_I'(\mathbf{r}) = (1 + \Delta)\psi_I(\mathbf{r}) \tag{1.54}$$

with $\Delta = \Delta(k, r_0, \theta_0, \pi)$,

$$\Delta(k, r_0, \theta_0, \pi) = 3 \frac{\exp(2ikr_0)}{kr_0^2} \cos^2\theta_0 \exp\big(2i\delta_1'(k)\big) f(k, \pi). \tag{1.55}$$

With this results it is finally possible to explicitly calculate the EXAFS function $\chi(k)$ taking into account that $\mu \propto |\langle i||z||\psi_I'\rangle|^2$. Therefore:

$$\chi(k)\frac{2}{kr_0^2}|f(k,\pi)|\cos\big(2kr_0+\varphi(k)+2\delta_1'(k)\big) \tag{1.56}$$

As a function of k, this is a sinusoidal oscillation multiplied by an envelope function.

Another crucial aspect to consider is the *de-excitation mechanisms*. When an atom possesses a core hole, it becomes inherently unstable and tends to relax spontaneously by filling the core hole with an electron from a higher level, thus reducing its energy.

1.3.4 De-excitation mechanisms

The rationale behind discussing atomic de-excitation processes will become apparent in the subsequent section on experimental analysis. Two primary de-excitation mechanisms exist:

1. In the *fluorescence mechanism*, the relaxation energy is emitted as an outgoing X-ray photon.

2. In the *Auger mechanism*, the relaxation energy is utilized to eject an electron (referred to as an *Auger* electron) from a higher level.

The energies associated with the fluorescence photons and Auger electrons are determined by the energy levels of the electrons and uniquely characterize the atomic species involved. The two de-excitation mechanisms are in competition. Their relative strengths is measured by the *fluorescence yeld*:

$$\eta_s = \frac{X_s}{X_s + A_s} \tag{1.57}$$

where s labels a given absorption edge (K, L_I), X_s and A_s are the emission probabilities of a fluorescence photon and an Auger electron, respectively.

The total de-excitation probability per unit time inversely correlates with the *core-hole lifetime*, typically ranging from 10^{-15} to 10^{-16} seconds.

The core-hole lifetime, denoted as τ_h, reflects the duration an atom retains a core hole before relaxation occurs. This period is influenced by two key factors: the depth of the core hole and the atomic number Z. A deeper core hole and a higher atomic number lead to a larger number of upper levels from which electrons can transition to fill the core hole. Consequently, this results in a shorter core-hole lifetime.

Due to the time-energy uncertainty relation, the core-hole lifetime τ_h is intrinsically linked to the energy width of the excited state, denoted as $\Gamma_h \approx \frac{\hbar}{\tau_h}$. This width, represented by Γ_h, plays a pivotal role in determining the resolution of X-ray absorption experimental spectra.

In practical terms, for a given absorption edge, an increase in the atomic number Z corresponds to a decrease in the core-hole lifetime τ_h and an increase in the energy width Γ_h. This dynamic relationship underscores the importance of core-hole lifetime in understanding and interpreting X-ray absorption spectra. For example, for the H atom, the lifetimes τ_h of electronic states are:

Level	τ_h(ns)
2p	1.6
3s	160
3p	5.4
3d	15.6
4s	230
4p	12.4
4d	36.5
4f	73

1.3.5 Main features of EXAFS

To conclude, *EXAFS* exhibits two key characteristics:

1. Atomic species selectivity, achieved by adjusting the X-ray energy to the corresponding absorption edge

2. Insensitivity to long-range order, owing to the short mean free path of the photoelectron, typically limited to about 10 Å.

These features render *EXAFS* a highly desirable method for probing local structural details.

In systems with numerous atomic constituents but lacking crystalline order, such as amorphous alloys or oxide glasses, the atomic selectivity of *EXAFS* enables the distinct examination of each component species' environment.

EXAFS serves as an invaluable tool for investigating systems wherein functional properties originate from individual atoms or small clusters embedded within a matrix of diverse atomic species. Such applications include the analysis of heterogeneous catalysts, active sites in biomolecules, impurities in semiconductors, and luminescent rare-earth atoms in crystals and glasses.

Moreover, *EXAFS* finds brilliant applications in studying the local structural properties of crystalline solids, which may differ from the average properties detected by diffraction.

Experimental Setup

A wide array of experimental methods for EXAFS analysis has arisen due to the sheer diversity of samples available for investigation. These samples span gases, solids, and liquids, featuring absorbing atoms with varying atomic numbers. The aim of this chapter is provide a general bird's eye view concerning the leading EXAFS experimental techniques. In particular, we will first delve into the formation process of synchrotron radiation, elucidating how this phenomenon arises. Following this, we will discuss the components and configuration of a typical experimental setup for Extended X-ray Absorption Fine Structure (EXAFS) studies. Finally, after a brief overview of the European Synchrotron Radiation Facility (ESRF), we will describe the specifics of the LISA beamline, detailing its experimental configuration and capabilities.

2.1 Synchrotron Radiation

When a charged particle is accelerated, its electromagnetic field can transport energy irreversibly out to infinity, in a phenomenon known as *radiation*. We are particularly interested in studying the radiation emitted by a charged particle moving with constant, relativistic velocity on a circular orbit with a curvature radius ρ. This phenomenon is called *synchrotron radiation*. To illustrate the main feature of synchrotron radiation, it is noteworthy to distinguish between the time t at which the radiation is observed and t', the time at which it was created by the moving charge. We adopt the geometric configuration depicted in Figure 2.1, where the particle's trajectory $\mathbf{R}(t')$ lies within the (x, z)-plane and passes through the origin at time $t' = 0$. An observer P receives the radiation at a fixed distance $\mathbf{r}_p$ from the origin, while the distance from the radiating particle to the observer, $\mathbf{r}(t') = \mathbf{r}_p - \mathbf{R}(t')$, varies over time. The observer is assumed to be located in a vertical plane at a tangent to the circular trajectory at the origin at an angle ψ above the level of the orbit.

The next set of results are obtained employing a few approximations[15]. First, let's assume that the radiation is emitted in a long magnet with a constant magnetic field, providing a constant curvature $1/\rho$ over a distance $l_r > 2\rho/\gamma$, with γ Lorentz factor. Secondly, the radiation is observed at a relatively large distance from the source $r_p \gg \rho/\gamma$. Finally, it is assumed that the particle moves with ultra-relativistic velocity, $\gamma \gg 1$. Under these approximations, the relation between the observation time t and the emission time t' becomes:

$$t = t' + \frac{r(t') - r_p}{c} \approx t' - \frac{\rho cos(\psi) sin(\omega_0 t')}{c} \tag{2.1}$$

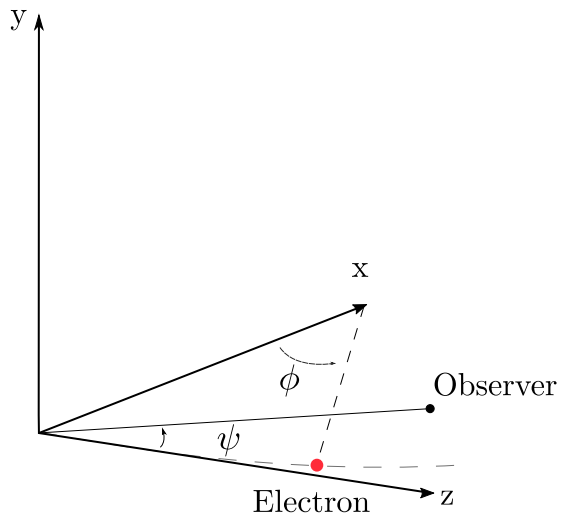

Figure 2.1: *The particle trajectory and the radiation geometry*

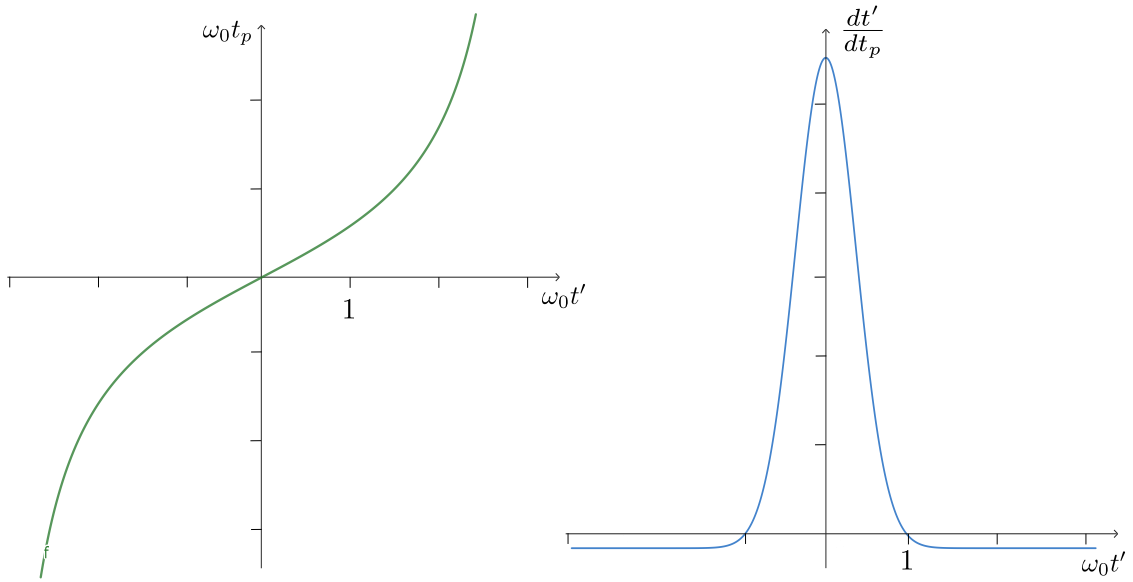

Figure 2.2: *Relation between the emission and observation time scales*

Where we have not considered the delay r_p/c, which is of little interest. By plotting $\omega_0 t_p$ against $\omega_0 t'$ (for a fixed value $\beta = 0.8$) we can see how the slope is small around the origin, which indicates that the radiation emitted over a time interval $\Delta t'$ is received by the observer within the smaller interval Δt_p (Figure 2.2). This result illustrates one of the most important physical principles of synchrotron radiation. Indeed, the length of the radiation pulse received is given by the difference in travel time between the particle and the photon for going from two point taken at arbitrarily small distance apart.

The expressions for the electric and magnetic fields $\mathbf{E}(t)$ and $\mathbf{B}(t)$ of a moving charge turn out to be:

$$\mathbf{E}(t) = \frac{e}{4\pi\epsilon_0}\left\{\frac{(1-\beta^2)(\mathbf{n}-\boldsymbol{\beta})}{r^2(1-\mathbf{n}\times\boldsymbol{\beta})^3} + \frac{\mathbf{n}\times[(\mathbf{n}-\boldsymbol{\beta})\times\dot{\boldsymbol{\beta}}]}{cr(1-\mathbf{n}\times\boldsymbol{\beta})^3}\right\}_{ret} \tag{2.2}$$

$$\mathbf{B}(t) = \frac{[\mathbf{n}_{\text{ret}}\times\mathbf{E}]}{c} \tag{2.3}$$

This field solution is known as the Liénard-Wiechert equation. The expressions that have to be evaluated at the earlier time t' are placed within curly brackets with the subscript 'ret' to ensure fluid readability. It is remarkable that the second term of (2.2), known as the acceleration field, depends on $1/r$, dominating the first term at large distances. Therefore, it is often referred to as the *far-field* term. The power radiated by the particle per unit solid angle is:

$$\frac{dP}{d\Omega} = \frac{r^2|\mathbf{E}|^2}{\mu_0 c}(1-\mathbf{n}\cdot\boldsymbol{\beta}) \tag{2.4}$$

Considering a particle that momentarily moving in the z-direction at ultra-relativistic velocity and using the angles θ and ϕ to describe the direction of emission, the following applies:

$$\frac{dP}{d\Omega} \propto \gamma^2 \frac{1 - 2\gamma^2\theta^2 cos(2\phi) + \gamma^4\theta^4}{(1 + \gamma^2\theta^2)^5} \tag{2.5}$$

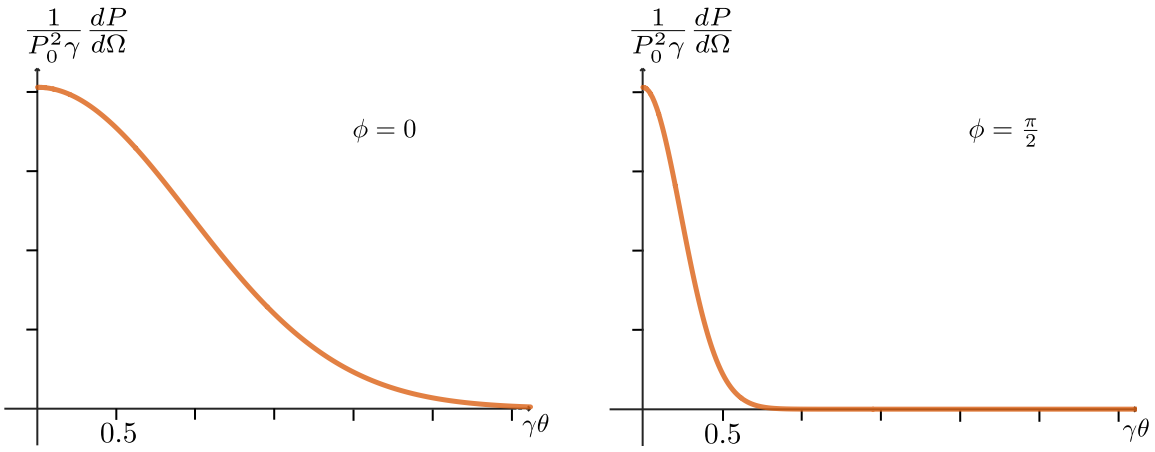

Figure 2.3: *Cuts through the power distribution for* $\gamma >> 1$

The form of the distribution depends on the product $\gamma\theta$ only and all angles θ scale as $1/\gamma$. The variance of the opening angle is:

$$\langle\theta^2\rangle = \int d\Omega \frac{dP}{d\Omega} = \frac{1}{\gamma^2} \tag{2.6}$$

Hence, due to relativistic effects, the radiation pattern is compressed into a narrow cone peaked in the forward direction. Thanks to this relativistic effect, we deal with extremely high fluxes on very small areas, even at distances of tens of meters from the storage ring.

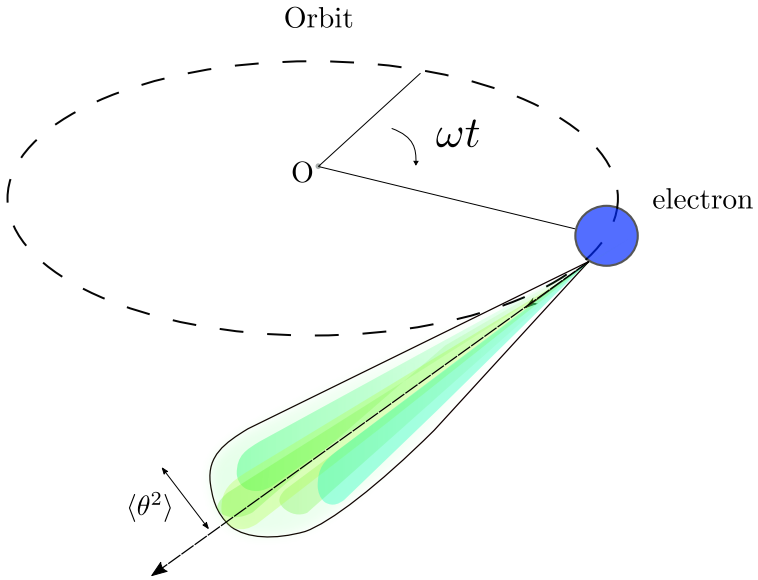

Figure 2.4: *Qualitative radiation pattern associated with charged particles in circular motion. It is characterized by distortion into a concentrated cone directed forward along the direction of motion(The figure was redrawn: it is based on Fig. 1.8 of [26])*

Because the charge makes a single traversal, a single pulse of radiation is emitted, and the observed spectrum will be continuous. By 2.2 it is possible calculate the Fourier transform of the radiated field:

$$\tilde{\mathbf{E}}(\omega) = \frac{1}{\sqrt{2\pi}} \int_{-\infty}^{\infty} \mathbf{E}(t_p) exp(-i\omega t) dt \tag{2.7}$$

The two field components are:

$$\tilde{E_x}(\omega) = \frac{e\gamma}{\sqrt{2\pi}\epsilon_0 c r_p} \left(\frac{3|\omega|}{4\omega_c}\right)^{1/3} Ai'\left(\left(\frac{3\omega}{4\omega_c}\right)^{2/3}(1+\gamma^2\psi^2)\right) \tag{2.8}$$

$$\tilde{E_y}(\omega) = \frac{ie\gamma\,(\omega/|\omega|)}{\sqrt{2\pi}\epsilon_0 c r_p} \left(\frac{3|\omega|}{4\omega_c}\right)^{1/3} \gamma\psi Ai'\left(\left(\frac{3\omega}{4\omega_c}\right)^{2/3}(1+\gamma^2\psi^2)\right) \tag{2.9}$$

expressed in terms of Airy function, where

$$\omega_c = \frac{3c\gamma^3}{2\rho} \tag{2.10}$$

is the critical frequency.

These results have two important consequences regarding the study of synchrotron radiation. Firstly, the radiation lying on the trajectory plane ($\psi = 0$) is linearly polarized, with the electric field vector also lying in the plane. Radiation observed at an angle

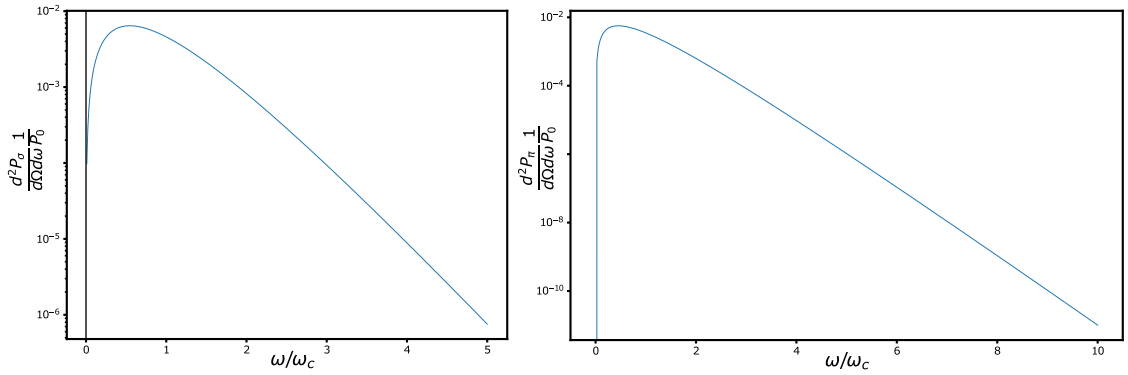

Figure 2.5: *The two modes of polarization of the radiated power. Both the graphs are plotted in logarithmic scale and are normalized by* $P_0 = (2r_0 m_0 c^2 \gamma^2)/(\pi\rho)$

$\psi \neq 0$ has some elliptical polarization, depending on whether ψ is positive or negative. In addition, the Fourier-transformed horizontal field $E_x(\omega)$ is large in the median plane $\psi = 0$ and has its maximum close to the critical frequency. As a consequence, we expect that the typical frequency of the spectrum will be truly 2.10.

The relevant physical quantity is the energy received by the observer per unit frequency band and solid angle. This quantity is called the *angular spectral energy distribution* or *density* of the radiation, and could be derived by taking an inverse Fourier transform of 2.8 and 2.9. The radiated power consists of two parts corresponding to the two modes of polarization:

$$\frac{d^2P_\sigma}{d\Omega d\omega} = \frac{2r_0 m_0 c^2 \gamma^2}{\pi\rho}\left(\frac{3\omega}{4\omega_c}\right)^{2/3} Ai'^2\left(\left(\frac{3\omega}{4\omega_c}\right)^{2/3}(1+\gamma^2\psi^2)\right) \tag{2.11}$$

$$\frac{d^2P_\pi}{d\Omega d\omega} = \frac{2r_0 m_0 c^2 \gamma^2}{\pi\rho}\left(\frac{3\omega}{4\omega_c}\right)^{4/3} \gamma^2\psi^2 Ai^2\left(\left(\frac{3\omega}{4\omega_c}\right)^{2/3}(1+\gamma^2\psi^2)\right) \tag{2.12}$$

This equation exhibits smooth behavior, as shown in Figure 2.5.
An useful quantity for experiments is the *spectral brightness* defined as the number of photons emitted per second in a spectral bandwidth $\Delta E/E = 0.1\%$ in a unit source area and per unit solid angle. The brightness is determined by the size of the source, which is given by the size of the electron beam and by the angular spread of the radiation. Another important experimental quantity is the product of the electron beam transverse size and the angular divergence, called *emittance*. In a storage ring, the latter quantity is constant. We distinguish two types of emittance, the horizontal and vertical ones. The former is measured in nanometer-radians, while the latter is normally a few percent of the horizontal one. In order to achieve high brightness, small emittance machines must be used.

2.2 EXAFS experimental techniques

The emergence of numerous experimental techniques for EXAFS measurement stems from the vast diversity of samples amenable to study. These encompass gases, solids, or liquids comprising absorbing atoms with high or low atomic numbers, distributed either uniformly in thin or thick specimens, or non-uniformly in thin layers atop bulk materials. Given its broad complexity across a wide range of factors, further study of the subject is warranted. Without presumptions, we could attempt to sketch a general overview regarding the *EXAFS experimental techniques*. The structure of an Extended X-ray Absorption Fine Structure (EXAFS) experiment is outlined as follows. Fig. 2.7 provides a schematic representation of the primary components involved in an X-ray absorption study. Typically, a distinction is made between the optical and experimental rooms (Fig. 2.6 and Fig. 2.7, respectively). As illustrated in Chapter 2.1, synchrotron radiation comprises a continuous spectrum of radiation (roughly depicted in Fig. 2.5). To achieve monochromatization in the X-ray region, two optical elements are employed: crystals and mirrors. X-ray mirrors serve dual purposes: they act as high-energy cut-off filters to eliminate unwanted radiation energy and as focusing devices. Given that the index of refraction at X-ray frequencies deviates little from 1 and so the refraction effects are very weak, total external reflection can be utilized. Therefore, by adjusting the incident radiation angle with the mirror, we can selectively filter the desired frequency range. Specifically, a portion of the radiation will be absorbed while the desired range will be reflected. This approach allows us to control and manipulate the X-ray beam to focus on specific energy ranges. Quantitatively, the real part of index of refraction is approximately determined by [26]:

$$n = 1 - \delta = 1 - \frac{\omega_p^2}{\omega^2} = 1 - \frac{\lambda^2 e^2}{\pi m c^2} \sum_a N_a Z_a$$

Here, ω_p is called *plasma frequency* and depends on the electronic density of the lattice. By applying Snell's law, we can calculate the critical angle θ_c:

$$\cos(\theta_c) = 1 - \delta$$

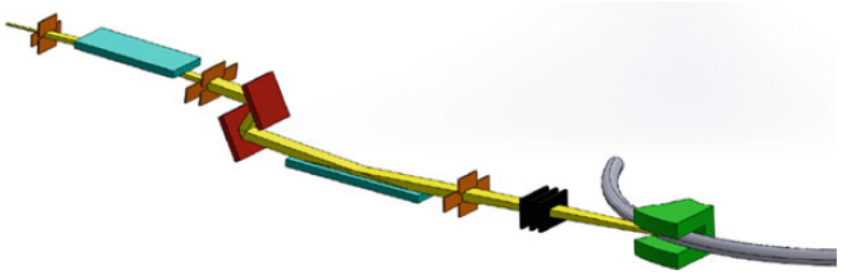

Figure 2.6: *Side view of the optical hutch of a generical beamline. (Figure* 3.2 *of [26])*

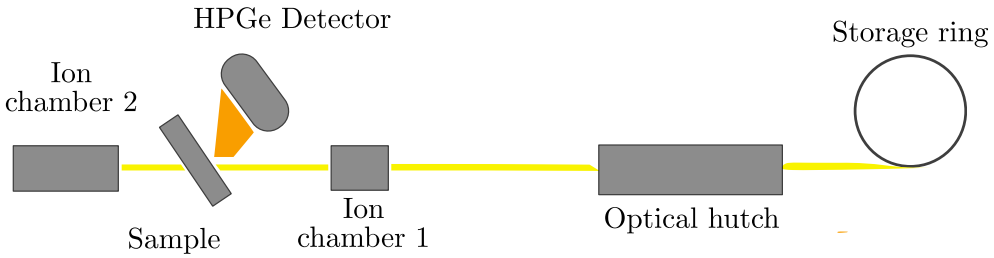

Figure 2.7: *Synthetic scheme of a general experimental room*

Since $\delta \sim 10^{-6}$, $\theta_c = \sqrt{2\delta}$; which means $\theta_c \sim 10^{-3} rad$. At a given angle $\theta < \theta_c$ there is a high energy cutoff given by:

$$E_c = \hbar\omega_c = \frac{\hbar\omega_p}{\theta}$$

The second application of X-ray mirrors is to collimate or to focus beam onto the following optical element or directly the sample. The best conditions are obtained with an elliptical or parabolic shape of the mirror surface.

The role of crystal, or *crystal monochromators*, is to select a narrow range from the broad spectrum of radiation's energy emitted by the storage ring. The condition for X-ray diffraction is expressed by Bragg's law [10]:

$$n\lambda = 2dsin(\theta_b) \tag{2.13}$$

Where d is the spacing of crystal lattice planes, λ is the central wavelenght reflected when the beam makes the angle θ_b wiht the Bragg planes. The integer n denotes the reflection order, and thus the selected multiple of λ. Since we are directly involved in isolate a narrow portion of spectrum, let's take into account the energy resolution of the monochromator. By differentiation of Eq. 2.13 we achieve:

$$\frac{\Delta E}{E} = \frac{\Delta\lambda}{\lambda} = \delta_r cot(\theta_b) \iff \delta_r > \delta_\omega$$

with $\delta_\omega \propto \lambda^2/sin(2\theta_b)$ is the Darwin reflection width, and δ_r is the inherent collimation of the radiation.

Hence, the resolution is determined by the angular range of incident radiation in the plane of scattering, and the extinction width δ_ω. The fraction of incident radiation's intensity within the bandwidth $\Delta\lambda$ that is reflected depends on a parameter ϵ typical of the system by the relation:

$$\frac{I_r}{I_0} = \epsilon\frac{\delta\theta_\omega}{\delta\theta_r} \iff \delta_r > \delta_\omega$$

Finally, a second reflection crystal is used to insure that the monochromatized beam always propagates in the same direction as the incident beam.

The level of detail needed for Extended X-ray Absorption Fine Structure analysis isn't extremely precise and to ensure accurate results and prevent data distortion, a resolution of at least 5 eV is recommended. Additionally, investing in higher resolution isn't beneficial because it hasn't uncovered any additional structural insights in most cases.

Now, let's consider the description of the detectors. As explained in Chapter 1.4, the objective of an X-ray absorption experiment is to measure the sample's absorption as a function of energy. This can be achieved in several ways, depending on the physical and chemical properties of the analyzed samples. The primary techniques involve either directly measuring the attenuation of the incident beam in a *transmission* experiment (typically used for concentrated samples) or measuring the *fluorescent radiation* or *non-radiative Auger* or *secondary electrons* (commonly employed with diluted samples). Firstly, an ion chamber filled with a mixture of gases (with absorption index μ) is employed to measure the incident intensity of the beam. This allows us to remove the effect of varying source intensity. With a source of brightness B and a mirror-monochromator system with a bandwidth $\Delta E(E)$, a solid angle collection of $\delta\Omega$ onto an area A with an efficiency $\epsilon(E)$, the photon flux I_0 incident on the chamber is given by:

$$I_0 = B\Delta E(E)\delta\Omega A\epsilon(E) \tag{2.14}$$

Since the detector absorbs a small fraction of incident intensity, the flux leaving the chamber will be:

$$I_{inc} = I_0 exp(-\mu x) \tag{2.15}$$

where x is the thickness of the gas mixture. Usually this radiation is collimated onto the sample and the products from matter-radiation interaction are detected by specific detectors capable of selecting only those information of our interest. To cancel out fluctuation of the source all measurements are made as a ratio of the signal to I_d, where I_d is:

$$I_d = I_0 - I_{inc} = I_0(1 - exp(-\mu x)) \tag{2.16}$$

When it comes to detecting fluorescent photons, various options are available, including scintillation detectors, non-dispersive solid-state detectors with or without absorption filters, or a combination of a curved crystal analyzer and a scintillation detector. Each of these detectors has its own resolution at 8 keV, which is approximately 2 keV for scintillation detectors, 200 eV for solid-state detectors, and 20 eV for crystal detectors. When evaluating these methods, factors such as solid angle acceptance and data rate capability also play a crucial role. Arrays of scintillators, solid-state detectors, or crystals can be used to increase the solid angle. The data rate capacity of the individual detectors is approximately 200000 counts/sec for the scintillation detectors, 40000 counts/sec for the solid-state detector, and essentially unlimited for the crystal. Let's now consider investigating the EXAFS signal from a uniform sample. We'll then analyze two different methods: transmission and fluorescence. Let's begin with the first method. The total absorption coefficient can be divided into the absorption of the atom of interest μ_A and that of the other atoms μ_B such that $\mu_T = \mu_A + \mu_B$. The intensity of transmitted photons detected by the second ion chamber is given by:

$$I_t = I_{\text{inc}} \exp(-\mu_T X_s) \tag{2.17}$$

Where X_s is the thickness of the sample. The total signal is the ratio I_d/I_t. Since we are only interested in the contribution of μ_A, specifically the modulations $\Delta\mu_A$ which carry the structural information, we write the EXAFS signal as:

$$S_t = \frac{\partial}{\partial \mu_A}\left(\frac{I_d}{I_t}\right)\Delta\mu_A = \Delta\mu_A X_s \frac{I_d}{I_t} \tag{2.18}$$

From this we can compute the noise, by the propagation of uncertainty:

$$N_t = \frac{I_d}{I_t}\left(\frac{1}{I_d} + \frac{1}{I_t}\right)^{1/2} \tag{2.19}$$

Then, maximizing the signal-to-noise ration with respect to absorption indexes, we obtain:

$$\frac{S_t}{N_t} = 0.736 \frac{\Delta\mu_A}{\mu_T} I_{inc}^{1/2} \tag{2.20}$$

Proceeding in the same way we obtain that for the case of fluorescence the intensity of fluorescent radiation in the detector with solid angle acceptance $\Omega/4\pi$ is given by:

$$I_f = I_{\text{inc}}\varepsilon_f \frac{\Omega}{4\pi}\frac{\mu_A(E)}{\mu_T(E) + \mu_T(E_f)} \tag{2.21}$$

Where ε_f is the fluorescence yield, E is the energy of the incident photon, and E_f is the characteristic fluorescence energy.

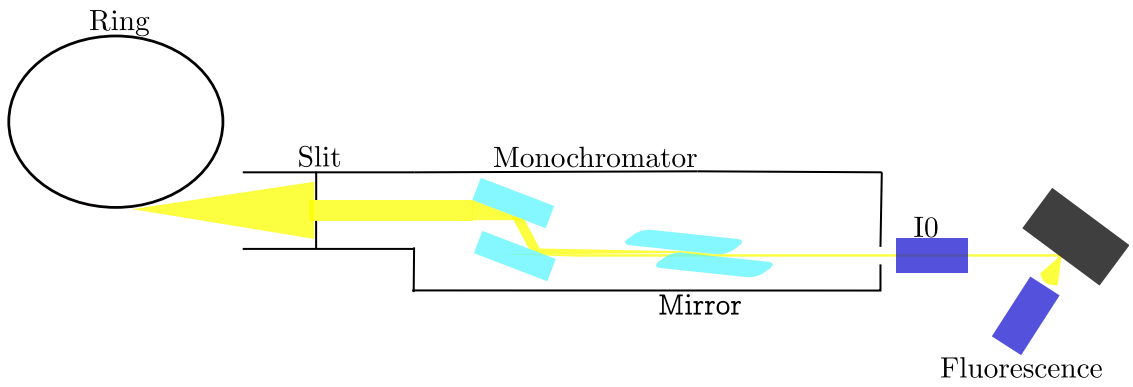

Figure 2.8: *A simplified model of a typical fluorescence measurement: Synchrotron radiation, depicted in yellow, passes through a monochromator that selects a specific frequency. After being adjusted by mirrors, the I0 detector measures the intensity of the beam just before it collides with the sample.[11]*

The EXAFS signal reads as:

$$S_f = \frac{I_{\text{inc}}}{I_d} \left(\frac{\varepsilon_f (\Omega/4\pi) \Delta\mu_A}{\mu_T(E) + \mu_T(E_f)} \right) \tag{2.22}$$

The S/N is then:

$$\frac{S_f}{N_f} = \left(\frac{I_{inc} \varepsilon_f (\Omega/4\pi) \mu_A(E)}{\mu_T(E) + \mu_T(E_f)} \right)^{1/2} \frac{\Delta\mu_A}{\mu_A} \tag{2.23}$$

Hence, generally speaking, if the total efficiency of the fluorescence detector $\varepsilon_f \Omega/4\pi$ is grater than μ_A/μ_T, the transmission technique is not preferred. More specifically, for atoms with atomic number $Z = 20$ to $Z = 100$, at greater than $10^{-2} - 10^{-3}$ diluition the fluorescence approach is preferred. Also for a low Z atom in a high Z material fluorescence is more favorable.

2.3 The European Synchrotron Radiation Facility

The European Synchrotron Radiation Facility, located in Grenoble, France, is a leading global research center equipped with cutting-edge high-energy synchrotron technology. Renowned as the brightest synchrotron light source worldwide, it serves as a premier facility for conducting both fundamental and innovation-focused studies in areas such as condensed and living matter science, with atomic resolution. Over 9000 researchers from across the world engage in experiments spanning physics, chemistry, and biology at the European Synchrotron. This success stems from collaborative efforts involving 21 partner nations, underpinning its global significance and impact in advancing scientific frontiers. The European Synchrotron comprises two primary structures: the experimental hall, which houses the 844-meter circumference rings and forty tangential beamlines, and a complex of laboratories and offices. Within the main ring, the linear accelerator electron gun (*linac*) and a smaller booster ring are utilized to speed up the electron beam to an operational energy of 6 GeV. Here, for 24 hours a day and as many days a year as its, it pulses out the most intense high-energy X-ray beams in the world.

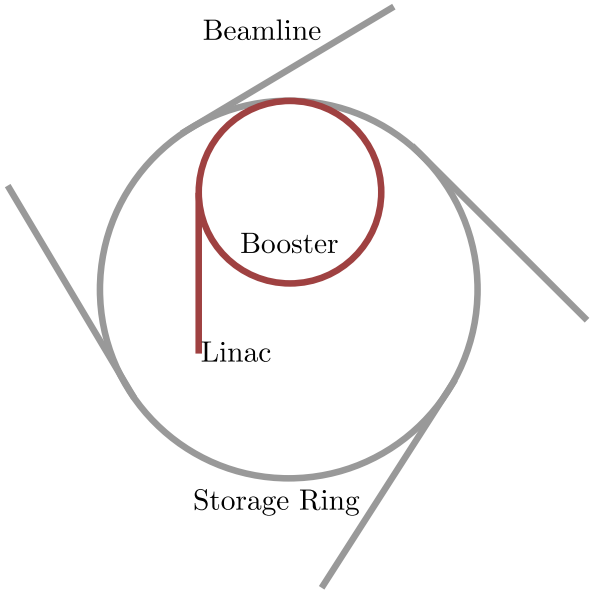

Figure 2.9: *Extremely terse depiction of ESRF main structure. Electrons are accelerated in the linear accelerator (linac) before entering the booster ring, where their velocity increases. Subsequentially, they are injected into the main storage ring, from which several beamlines extend.*

In 2015, the Extremely Brilliant Source (ESRF-EBS) Project started, initiating the construction of a new storage ring within the existing infrastructure. The project was dedicated to designing and constructing the ultimate storage ring, with the goal of achieving an equilibrium emittance approaching the diffraction limit. In particular an equilibrium emittance of about $150pm \times rad$ has been reached, replacing the previous one of about $4.0\,\text{nm} \times \text{rad}$.

Figure 2.10: *Aerial view of the European Synchrotron Radiation Facility (ESRF) ring in Grenoble, France. [17]*

2.4 Beamline Instrumentation at LISA

LISA [2] (Linea Italiana per la Spettroscopia di Assorbimento X), also known as the Italian beamline, represents a dedicated facility at the forefront of synchrotron research, designed to address the growing demand for precise and high-intensity X-ray beams in scientific investigations. In particular, LISA plays a central role in the field of X-ray absorption spectroscopy (XAS) and related techniques. LISA comprises three primary compartments, as depicted in figure 2.11: the optic hutch (OH), containing essential optical components, and two experimental hutches (EH1 and EH2).

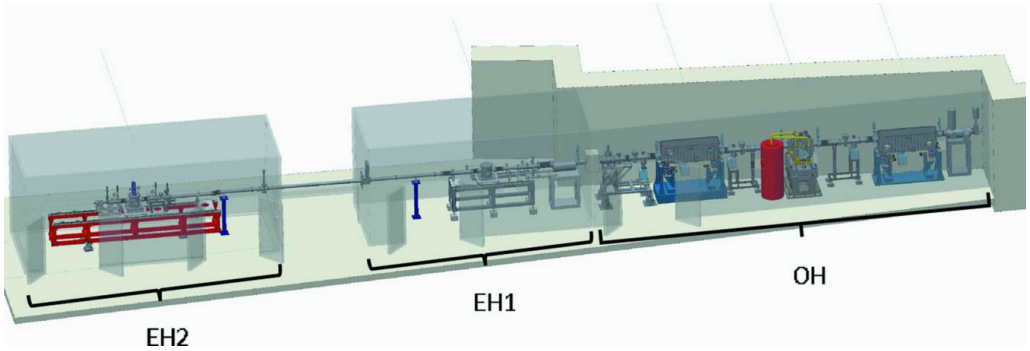

Figure 2.11: *Overview of the LISA beamline layout, highlighting the presence of three primary areas. Positioned approximately 28m from the radiation source, the right area is designated as the optics hutch (OH). Further down the beamline, the first experimental hutch (EH1) is located at a distance of 37m, while the second experimental hutch (EH2) is situated 49m away from the source.*

The X-ray radiation reaching LISA originates from a bending magnet within the ESRF ring, featuring an electron beam energy of 6.03 GeV and a typical current of 200 mA. The magnet generates a magnetic field of 0.85 T, resulting in a critical energy of 20.6 keV. The source has a horizontal dimension of 78 µm and a vertical dimension of 36 µm, with emittance values of 8.5 nm (horizontal) and 25 pm (vertical). Concerning the optics hutch, the layout of this room is shown in figure 2.12. Alongside a vacuum vessel containing a set of attenuators that reduce thermal load, the first optical element is the collimating mirror M1 (labeled as number 2 in Fig. 2.12). It is positioned approximately at 24.9 meters from the source and has a cylindrical shape, consisting of a single-crystal Silicon substrate. Half of the mirror is coated with a Platinum stripe, while the other half exposes the Silicon. The mirror's radius of curvature can be adjusted using a stepper motor. As we move to the left, we encounter the monochromator, labeled as number 4 in figure 2.12. Its function is to separate polychromatic radiation into individual wavelengths (with an energy resolution $\Delta E/E \leq 10^{-4}$ for the Si(111) crystal pair, enabling the selection of a narrow band of these wavelengths. It operates as a fixed-exit system and is equipped with two sets of flat silicon crystals: one set cut along the (311) planes and the other along the (111) planes. The first crystals have dimensions of 40mm (width) × 48 (thickness) ×

140mm (length) whereas the second crystals are 40mm × 37mm × 57mm. Both pair of crystals are cooled by liquid nitrogen fed by an external cryocirculator (labelled as number 5 in Fig. 2.12. The operational angular range spans from 3.5 to 51 degrees, enabling access to energy ranges of 2.5 to 32.5 keV with the Si(111) crystals, 4.9 keV to 72 keV with the Si(311) crystals, and 7.6 to 97 keV with the Si(333) reflection (corresponding to the third harmonic of Si(111)). The monochromator motion is controlled by SPEC, a UNIX-based software package for instrument control and data acquisition. The Bragg angle, defined by the cumulative steps of the Bragg motor, is the primary variable to define the nominal energy (based on the crystal type). It is necessary apply an offset to the Bragg angle's value during the energy calibration process at the start of experiments for 'recise energy determination. Subsequently, the counts from the main Bragg encoder are utilized by an offline routine to establish the final precise energy scale.At a distance of 31.6m from the source, we encounter the second mirror M2 (number 7 in Fig.2.12). It is a double toroid and consist of a single substrate of crystalline silicon with two parallel cylindrical channels, one oh which is coated with Platinum.

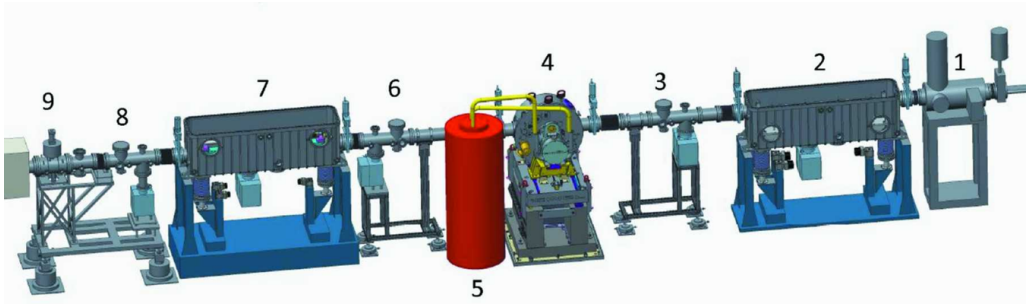

Figure 2.12: *Side view of the optics hutch. The numbers label the different elements: 1, chamber with principal slits, attenuators and white beam monitor; 2, first mirror M1; 3, 6, 8, beam monitors; 4, monochromator; 5, cryocirculator; 7, second mirror M2; 9, beam shutter.*

The first experimental hutch (EH1), depicted in figure 2.13a, is equipped for experiments utilizing a non-focused beam with dimensions of approximately $1mm \times 2mm$. It includes a vacuum vessel housing low-energy harmonic rejection mirrors (labeled as 1) and a vacuum chamber with a manipulator for the sample. Preceding and following the sample manipulator are two ion chambers, denoted as I_0 and I_1, respectively. These ion chambers have electric field values of approximately $1kVcm^{-1}$ and lengths of 150mm and 400mm, respectively. The signals from these chambers are read by picoamperometers, and their output is sent to the data acquisition computer via voltage-to-frequency converters. These detectors can be filled with nitrogen, argon, or krypton at pressures ranging from 0.1 to 1 bar.

The second experimental hutch (EH2), shown in figure 2.13b, accommodates all instrumentation necessary for experiments utilizing a focused beam and is centered on the focal spot of the second mirror of the optic hutch (M2), at 49 meters from the source (validating the approximations done in Chapter 2.1). The data acquisition setup in EH2

consists of three ion chambers (I_0, I_1 and I_{ref}, respectively labelled as 2, 4, 6 in Fig.2.13b) and each measuring 100 mm in length, similar to the ones mentioned previously. To detect sample fluorescence, two sets of high-purity germanium detectors (one comprising 12 elements and the other containing 13 elements) are used. Moreover a four-channel silicon drift detector (SDD) is utilized for energy ranges ($< 15KeV$). Experiments are conducted within vacuum chambers (3) equipped with manipulators capable of accommodating either cold finger or cold chamber cryostats, offering a temperature range spanning from room temperature down to 20K. Alternatively, experiments can also be conducted using a high-temperature reactor cell known as *microtomo*.

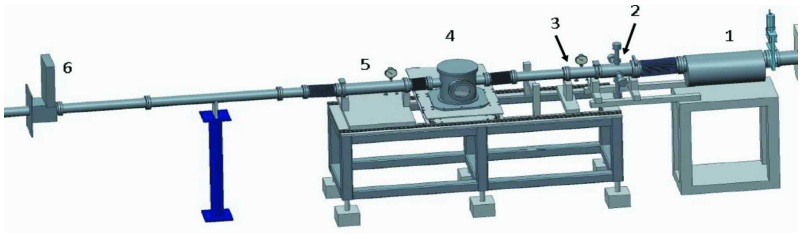

(a) *Side view of the EH1 cabin. Numbers label the various elements: 1, chamber with low-energy mirrors; 2, slits; 3, ion chamber I_0; 4, sample chamber; 5, ion chamber I_1; 6, shutter.*

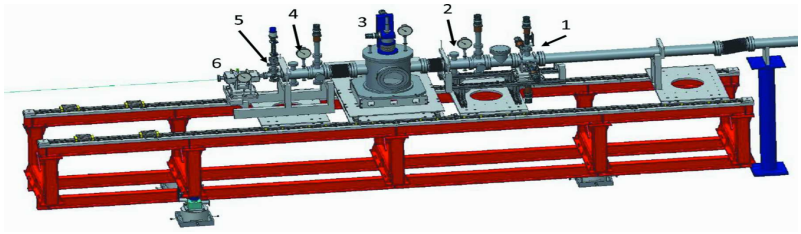

(b) *Side view of the EH2 cabin. Numbers label the various elements: 1, slits; 2, ion chamber I_0; 3, sample chamber; 4, ion chamber I_1; 5, reference foils holder; 6, ion chamber I_{ref}.*

Figure 2.13: *A schematic depiction of the experimental hutches is provided. The top figure (a) illustrates the layout of EH1, while the bottom figure (b) depicts the experimental hutch EH2*

Finally, let's consider the beamline's performance by presenting the key findings from focused studies assessing its effectiveness. First of all, the energy resolution. This primarily depends on several factors, including the crystal planes used for the data collection, the thermal bump and the effective collimating power of the first mirror. Through experiments conducted using Si(111) crystals at the Bromine K-edge (13474 eV), was achieved the minimum resolution with a radius of curvature of approximately 30 m. The optimum radius was found to be the same if using the Platinum or Silicon side of the mirror and so, by the power of the close vicinity between theoretical and experimental results, we are allowed to neglect the principal source of resolution degradation (namely, the crystal

mechanical stress). The measured value of ($\sim 1.7 \pm 0.1$) eV closely aligns with the intrinsic resolution of the Si(111) crystal, which is 1.75 eV at this energy threshold. In terms of the flux available on the sample, experiments conducted using Nitrogen or Argon within the ion chamber revealed the results depicted in figure 2.14. The measured data satisfactorily align with the theoretical calculations. The experimental data concerning the beam size yields a size of $\sim 170\mu m \times 180\mu m$, in fair agreement with the theoretical predictions, which are $\sim 120\mu m \times 180\mu m$. Furthermore, with the new EBS source it is possible to achieve a smaller beamsize of $\sim 40\mu m \times 70\mu$ as depicted in figure 2.15.

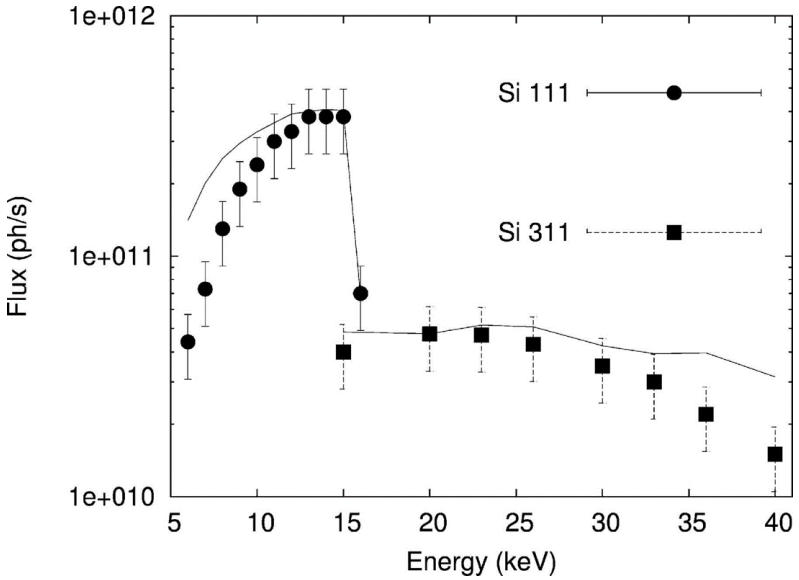

Figure 2.14: *Comparison of experimental data (with error bars) and theoretical calculations depicting the flux available on the sample under focusing conditions. Measurements were conducted using a Platinum mirror for Si(311) data and a Silicon mirror for Si(111) data.*

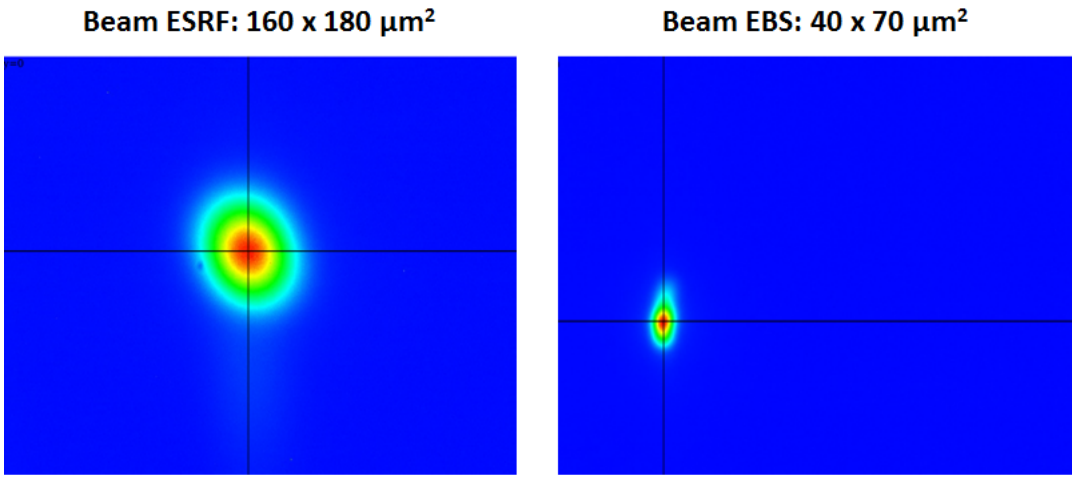

Figure 2.15: *Comparison of previous beam size (left image) and after-EBS beam size (right image). It is clear the quality improvement.*

Development and Implementation of an Innovative Data Analysis Program

The aim of this work is to study a new mechanism for X-ray Absorption Fine Structure data treatment, using fluorescence as the analysis technique. Currently, at the LISA beamline, the acquisition software extracts the EXAFS signal from a predefined region of the fluorescence spectra without saving the entire spectrum, specifically from the integrated intensity within a fixed region of the domain. This technique does not allow a posteriori corrections of the Region of Interest (ROI). The purpose of my work, described in this chapter, is the development of two software programs that address this limitation. Firstly, the raw data are customized into a NeXus file format, which is a typical way to organize massive quantity of scientific data. Secondly, a data analysis program allows the user to select a region of integration as desired. Furthermore, for the latter, a supplemental routine has been developed to allow post-analysis corrections such as dead time correction and the correct normalization parameters.

3.1 Experimental Setup and Data Collection

In order to understand in depth the developed software, let's summarize the main features of the experimental setup we are interested in. At low concentrations, recording X-ray absorption spectra in fluorescence excitation mode is more sensitive than in transmission mode but, for dilute samples, the fluorescence signal is often obscured by scattered X-rays and matrix filter fluorescence. To avoid considering this background while maintaining a large angular acceptance and high count rate capability, solid-state energy-resolving detectors are often used in fluorescence EXAFS measurements. Specifically, *intrinsic germanium* or *high-purity germanium* (HPGe) detectors are employed.

3.1.1 High-Purity Germanium detectors

The first advantage of using this type of material concerns the thickness of the depletion region in the detector. With germanium of normal semiconductor purity, achieving depletion depths beyond 2 or 3 millimeters is difficult, even when applying bias voltages near the breakdown level. Indeed, the thickness of depletion region is given by:

$$d = \left(\frac{2\varepsilon V}{eN}\right) \tag{3.1}$$

Where N is the impurity concentration and V is the reverse bias voltage. Quite the opposite, by reducing the impurity concentration to approximately 10^{10} atoms per cubic centimeter, a depletion depth of 10 mm can be achieved using a reverse bias voltage of less than 1000 V. A typical configuration for an HPGe detector made from π-type germanium is illustrated in figure 3.1. The term π-type refers to germanium that contains a low concentration of acceptor impurities, such as aluminum, making the material slightly p-type. The detector consists of a germanium disk with electrical contacts applied to its two flat surfaces. Typically, one side of the junction is formed by a heavily doped n^+ layer, achieved through lithium evaporation and diffusion onto one surface of the wafer.

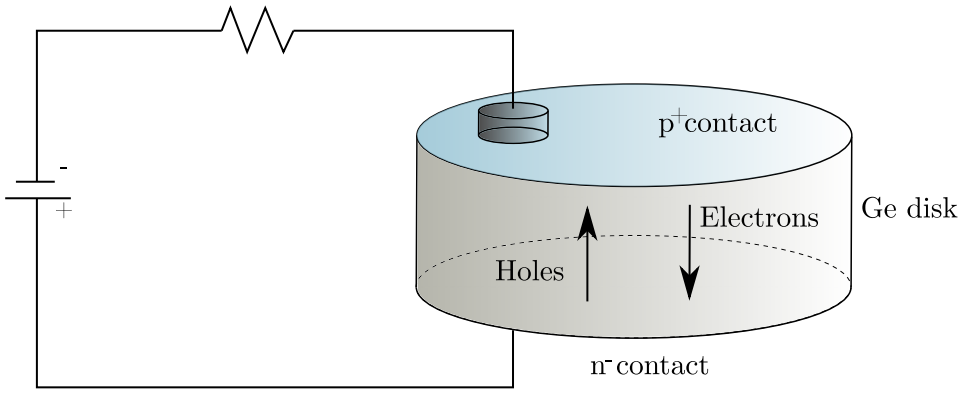

Figure 3.1: *Configuration of a planar HPGe detector*

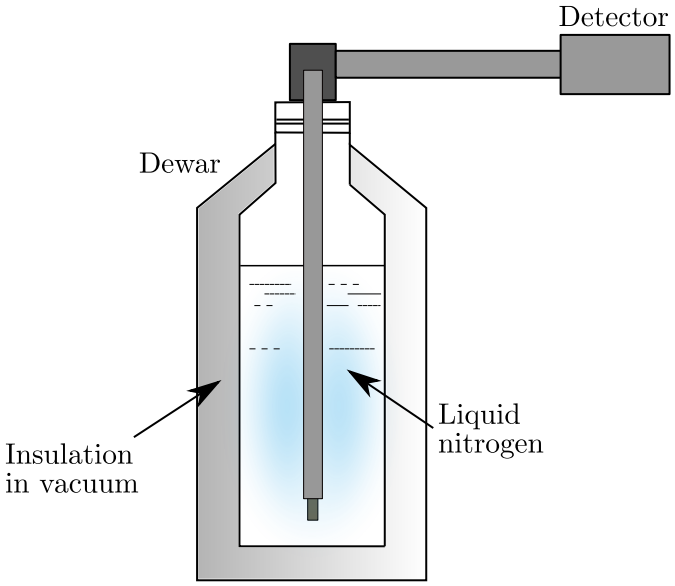

Figure 3.2: *Diagram showing the location of a HPGe detector within its vacuum capsule. In this design, the capsule can be connected, without using vacuum pumps, to a variety of cryostats or cryostat-dewar assemblies.*

The detector depletion region is formed by reverse biasing this $n^+ - p$ junction. On the opposite side of the junction, a p^+ contact is created by ion implantation of acceptor atoms. This configuration is particularly significant for detecting low-energy X-rays, as the implanted layer can be made very thin to act as an entrance window for weak radiation. High-purity germanium detectors are used in a state where the entire thickness of the detector becomes depleted, known as *fully depleted operation*. This condition arises when the depletion region spans almost the entire thickness of the detector material. In this configuration, maintaining a high electric field throughout the detector volume helps to enhance the timing response of the detector.
Due to its small bandgap (0.7 eV), germanium detectors cannot operate at room temperature due to significant thermally-induced leakage currents that would occur. Typically, the detector temperature is reduced to 77 K using an insulated *dewar*. This dewar maintains a reservoir of liquid nitrogen in thermal contact with the detector. Therefore, the detector must be housed in a vacuum-tight cryostat to inhibit thermal conductivity between the crystal and the surrounding air. At this temperature, saturated electron velocities are reached at a minimum field of about 10^5 V/m , but field strengths three to five times larger are required to fully saturate the hole velocity.

3.1.2 Pulse Shaping

Let's concentrate on pulse processing, specifically on extracting information from pulses generated by radiation detectors. By focusing on this subject, we gain a deeper understanding of the measurement process, which is crucial for grasping the developed software. In fact, the software extracts information from raw data, making it essential to comprehend the presence of systematic flaws during the acquisition chain. The basic components in a typical signal processing chain are shown in figure 3.3. When a radiation interacts with the detector, electron-hole pairs are created and move under the applied electric field to the appropriate electrodes, generating a current pulse by their motion. In particular, the detector material releases a total electric charge $Q = E/\varepsilon$, where the material constant ε is the amount of energy needed to form an electron-hole pair, and E is the energy of the incident photon. In dealing with these type of pulses, it is often desiderable to change the shape of the pulse in some predetermined fashion. Additionally, the total charge is too small to be sensed directly, so the current is sent to a *preamplifier*, an interface between the detector and the subsequent processing electronics. The aim of the preamplifier is to integrate the transient current pulse to produce a voltage step proportional to Q. Q is integrated onto the preamplifier's feedback capacitor C to produce the voltage $V = Q/C = E/(\varepsilon C)$. Measuring the energy E of the X-ray therefore requires a measurement of the voltage step V in the presence of the amplifier's noise σ. Figure 3.4 is a simplified schematic of a preamplifier, where C is discharged through the switch S from time to time when the preamplifier's output voltage gets so large that it behaves nonlinearly.

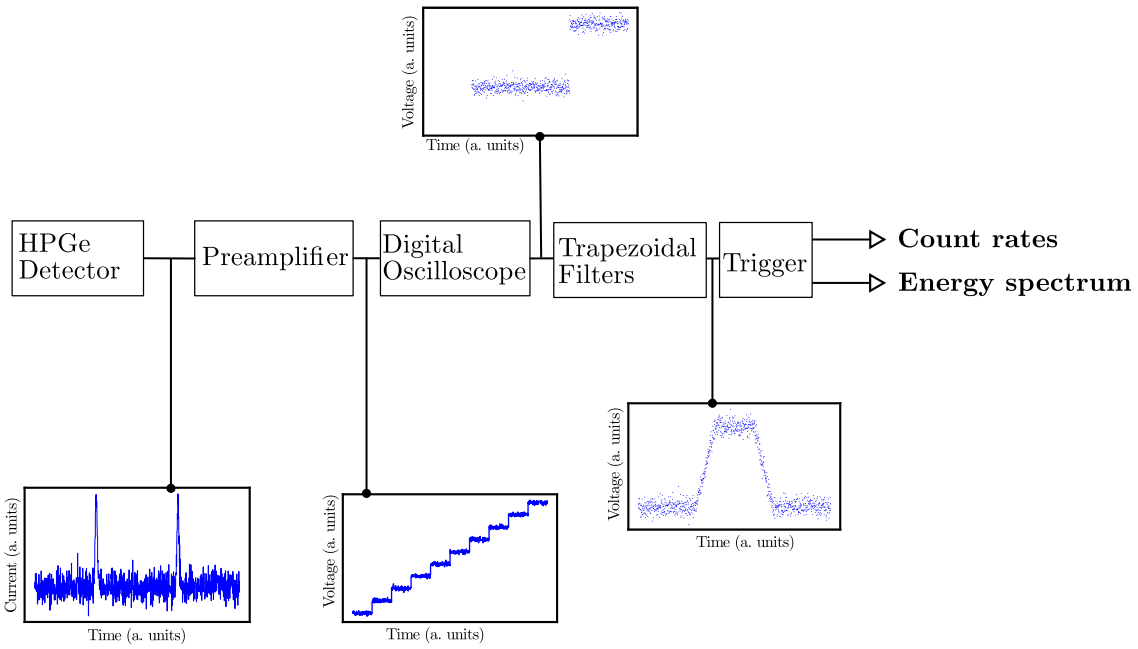

Figure 3.3: *Schematic diagram of the detector and the electronics*

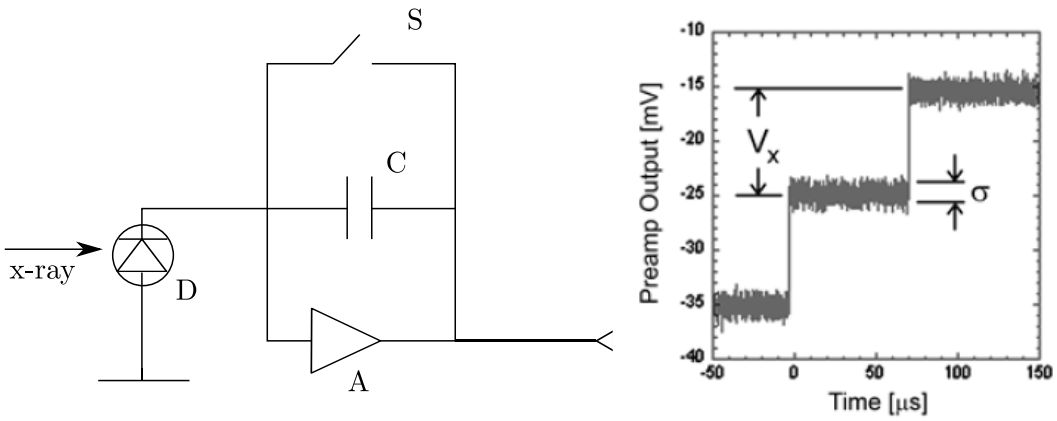

(a) (b)

Figure 3.4: *On the left (a) is a simplified version of the preamplification circuit. Letter D represents the HPGe diode, C indicates the capacitor, A is the amplifier, and S is the switch (which could sometimes also be a transistor). On the right (b), the output on absorption of x-rays converted into voltage.*

The shaping amplifier, or pulse-processing filter, transforms the signal from the preamplifier into a form suitable for measurement. The basic logic consists in converting the preamp output steps into either triangular or semi-Gaussian pulses whose amplitudes (with respect to their baselines) are then proportional to Q and thus to the x-ray's energy. To avoid overlapping pulses that could distort the measurements, the amplifier must quickly return to its baseline after each pulse. We are particularly interest in the study of digital filtering. Here the signal from the preamp has been digitized by a digital oscilloscope at $\sim 10MHz$. Referring at figure 3.5, the obvious approach to determining V is to take some sort of average over the points before the step (L) (the "Gap" region G is omitted because the signal is changing rapidly here) and subtract it from the value of the average over the points after the step. Thus the value V_k for the k-step may be found from the equation:

$$V_K = -\sum_{i(\text{before})} w_i v_i + \sum_{i(\text{after})} w_i v_i \tag{3.2}$$

When the weighting values are constant, one obtains *trapezoidal filters*. The result of applying such a filter is shown in figure 3.5. The filter output is clearly trapezoidal in shape and has a risetime equal to L, a flattop equal to G, and a symmetrical falltime equal to L. Two type of trapezoidal filters could be distinguished: *fast* and *slow*. The slow filter averages out the most noise and can thus detect smaller x-ray steps, but has a response that is much slower. The fast filter is used solely for x-ray detection, which means that

successive pulses that would pile-up in the slow filter can be resolved in the fast filter and rejected from the spectrum (Fig.3.6). Hence, after an x-ray has been detected, the step height is only measured at the slow filter output. In addition, not all values of V are valid; only those corresponding to filtered pulses that are sufficiently well separated in time from preceding and succeeding pulses will be effective measures of their associated x-ray energy. In figure 3.6 the pulses are separated by intervals of 3.2, 1.8, 5.7, and 0.7 μs, respectively. The fast filter has a risetime of $0.4\mu s$ with no gap, whereas the slow filter has a risetime of $2.0\mu s$ with a gap of $0.4\mu s$. The first kind of pileup is *slow pileup*, which refers to pileup in the slow channel. This occurs when the rising (or falling) edge of one pulse lies under the peak of its neighbor. Thus, peaks 1 and 2 are sufficiently well separated so that the leading edge (point 2a) of peak 2 falls after the peak of pulse 1. To be detected as separate by the slow channel, two pulses must be separated by at least an interval of L + G/2. Consequently, peaks 2 and 3 are seen to pile up in this example. Pulses 4 and 5 are so close together that the output of the fast filter does not fall below the threshold between them, and they are detected by the pulse detector as only a single x-ray pulse. To reject as many of these fast channel pileup cases as possible, the fast channel pileup test has been implemented. Since the rise time of the preamplifier pulses is independent of the x-rays' energies, and thus the width of the peak will be energy-independent, the width will never exceed some maximum value, "Maxwidth". Thus, if the width of the fast filter output pulses is measured at the threshold and found to exceed Maxwidth, then fast channel pileup must have occurred.

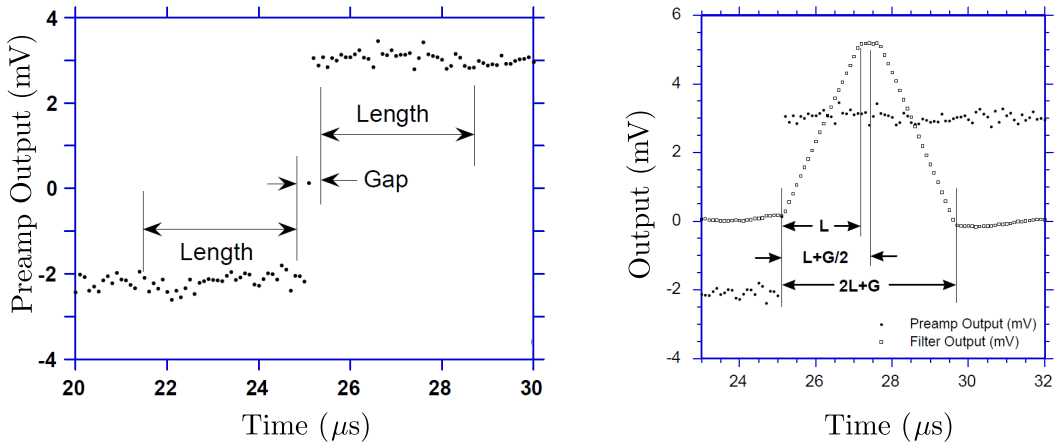

Figure 3.5: *On the left, we observe the output of the reset-type preamplifier, which is digitized at approximately 10 MHz. This step represents the detection of a photon by the detector. On the right, this signal is processed by a trapezoidal filter.[30]*

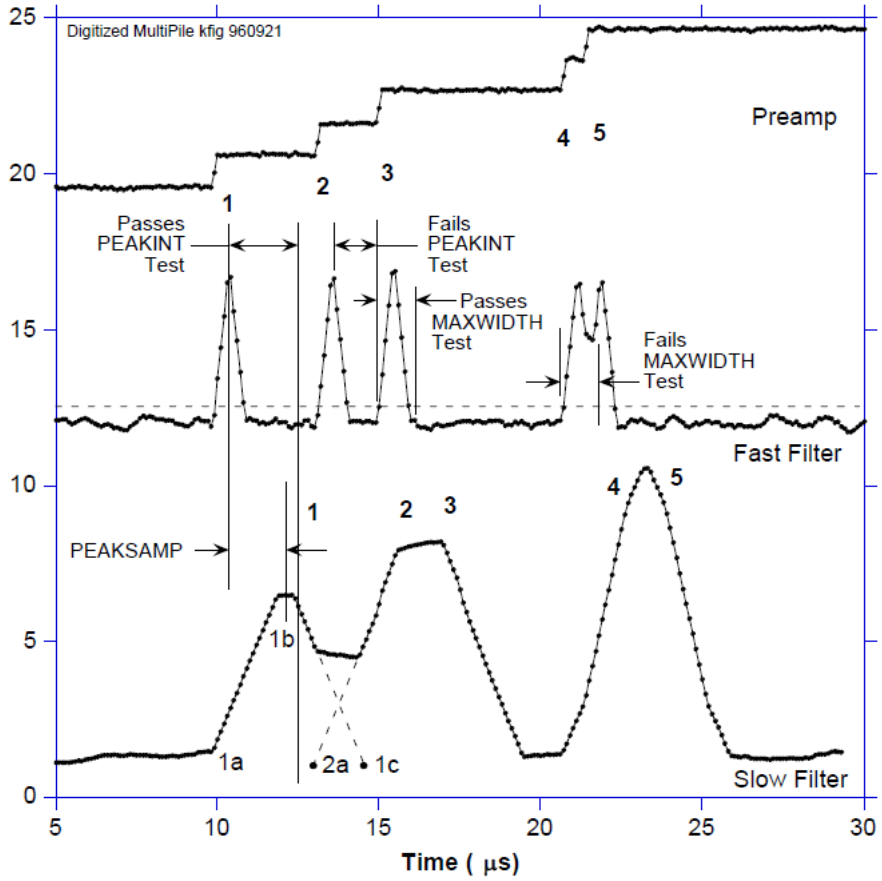

Figure 3.6: *A sequence of 5 x-ray pulses separated by various intervals to show the origin of both slow channel and fast channel pileup and demonstrate how the two cases are detected by the electronics.* [30]

As mentioned earlier, we aim to capture a value of V for each detected X-ray and use these values to construct a spectrum. Once an X-ray is detected, the step height is measured at the slow filter output. Depending on the level of decimation, one of two methods is used to capture the slow energy filter output to ensure the best measurement of V. For decimations 2, 4, and 6, the slow filter output is observed over a finite time interval around its peak, and the highest value within that interval is recorded. For decimation 0, the slow filter is sampled at a fixed time interval after the pulse is detected by the fast filter. Figure 3.7 (a) is a significant example of an acquired spectrum during a fluorescence experiment. Specifically, it represents an energy source scan. For each source energy, there is a count rate spectrum (Fig. 3.7(b)), which is obtained by horizontally sectioning the two dimensional plot. This latter is exactly the energy spectrum that the pulse shaping chain extracts.

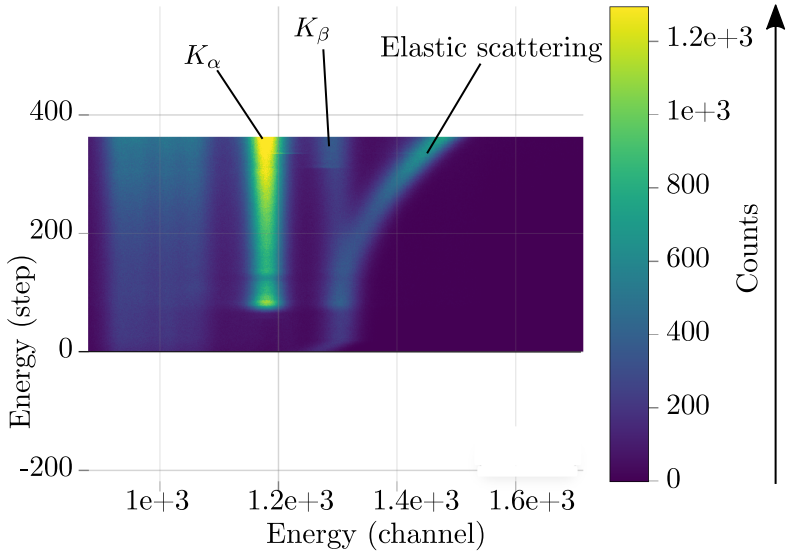

(a)

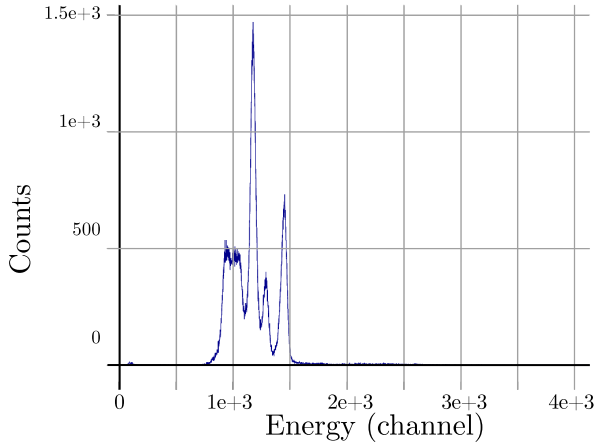

(b)

Figure 3.7: *(a) The two-dimensional plot illustrates the findings of an X-ray absorption spectroscopy experiment conducted with copper foil at the LISA Beamline. The plot on the x-axis illustrates the fluorescence photon energy, expressed as the channel of the detector, while the y-axis depicts the incident photon energy, expressed as the steps of the encoder. The color gradient indicates the count rate of the detected beam. The most prominent feature is the K_α line, which appears as a bright, straight line. Adjacent to it is the K_β line, which is less prominent. Additionally, the curved signal in the heatmap corresponds to the elastic. (b) Energy spectrum showing the number of photons detected by the slow filter, based on the voltage value associated with each photon's detection*

3.1.3 Input count Rate, Output Count Rate and Dead Time

During data acquisition, X-rays are absorbed by the detector at a certain rate, referred to as the *true input count rate* (ICR_t). However, due to the phenomenon of pile-up, because of the finite time of detection and filtering, not all of these X-rays will be detected by the detection circuitry. Consequently, the circuitry reports a *measured input count rate* (ICR_m), which is lower than the true input count rate (ICR_t). Some fraction of the detected x-ray will have their value of V captured and placed into the spectrum. This number is the *output count rate*(OCR). Once the main characteristics of the detectors have been described, it is essential to analyze a typical systematic error associated with the radiation detection. I'm referring to *dead time*, which is the minimum amount of time τ that must separate two events for them to be recorded as two separate pulses. It is interesting to model the dead time behavior of counting systems, in order to propose a correction method that will be the central argument of the next paragraph. Let's suppose that a fixed time τ follows each true event that occurs during the *live period* of the detector. True events that occur during the dead period are lost and, in addition, are assumed to extend the dead time by another period τ following the lost event. This model is commonly named *paralyzable* response and is depicted in figure 3.9. In the discussion that follows, we adopt the definitions where n is the true interaction rate and m is the recorded count rate. In particular, this latter, is identical to the rate of occurrences of time intervals between true events that exceed τ. The distribution of intervals between random events occurring at an average rate n is:

$$P_1(t)dt = n\exp(nt)dt. \tag{3.3}$$

The probability of intervals larger that τ can be obtained by integrating between τ and ∞:

$$P_2(\tau) = \int_{\tau}^{\infty} P_1(t)dt = \exp(-n\tau) \tag{3.4}$$

The rate of the occurrence of such intervals is then obtained by simply multiplying the above expression by the true rate n:

$$m = n\exp(-n\tau) \tag{3.5}$$

As shown in the plot of the observed rate m versus the true rate n (Fig. 3.8), a paralyzable model reaches a maximum at $n = 1/\tau$, after which the exponential term dominates over the linear term. We are particularly interested in the region of domain where the losses are grater than 30 or 40 %. Here the true rate becomes very sensitive to small changes in the measured rate and the assumed system behavior.

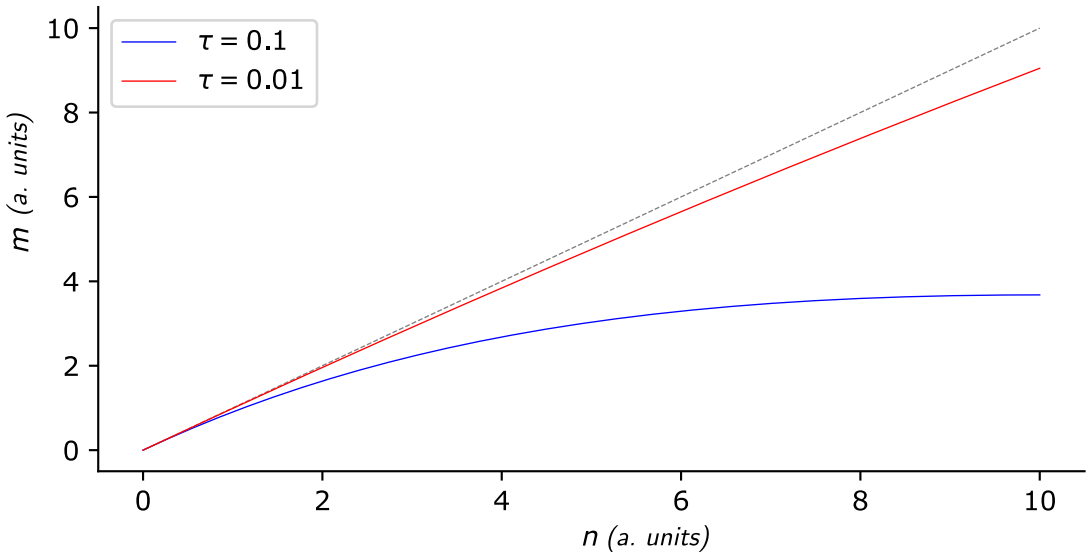

Figure 3.8: *Variation of the observed rate m as a function of the true rate n for two values of dead time, compared with the ideal case depicted as dashed line. As expected, the smaller the τ the more efficient the detector.*

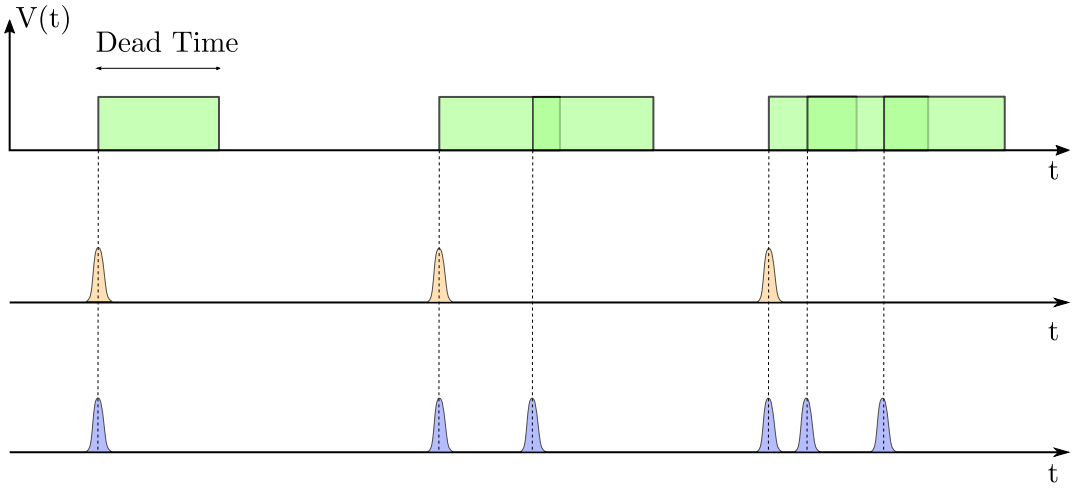

Figure 3.9: *Illustration of the dead time model with a paralyzable response. The top plot describes the response time of the detector. The middle graph shows the behavior of a real detector response subject to dead time. The bottom graph simulates a perfect detector in the case where the dead time can be neglected*

3.1.4 Fluorescence Analysis and Issues with the Region of Interest

As discussed in the previous paragraph, during a fluorescence experiment, the experimental apparatus can effectively construct the energy spectra of the radiation emitted by the analyzed sample after interaction with the incident monochromatic photon beam. By progressively increasing the energy of the beam source, the fluorescence intensity peak for each energy level can be computed by integrating the fluorescence spectrum within a specified region (the Region of Interest). Therefore, as described in chapter 2.2, it is possible to extract the EXAFS signal by a fluorescence spectra by computing the ratio between the intensity of the fluorescence peak and the incident radiation as a function of the incident beam energy. However, as depicted in figure 3.7(a), for each source energy, the fluorescence spectra include not only fluorescence peaks but also Compton or Rayleigh signals. Furthermore, if the EXAFS signal of a chemical element with a low atomic number needs to be studied, the spectral lines K_α and K_β would be very close to each other in terms of energy. Hence, it is indispensable to develop a method that allows for the separation of experimental signals from different physical origins. This way, we can focus solely on the phenomena of interest, discarding unnecessary data. The method provided by the LISA Beamline begins with acquiring a fluorescence spectrum at a source energy above the edge energy. This test provides information on the shape of the peaks of interest, allowing us to define an appropriate region of interest. After this, the energy scan in the neighbourhood of the edge energy commences, and the system is programmed to automatically calculate the fluorescence line count rate within the predefined interval for each energy.

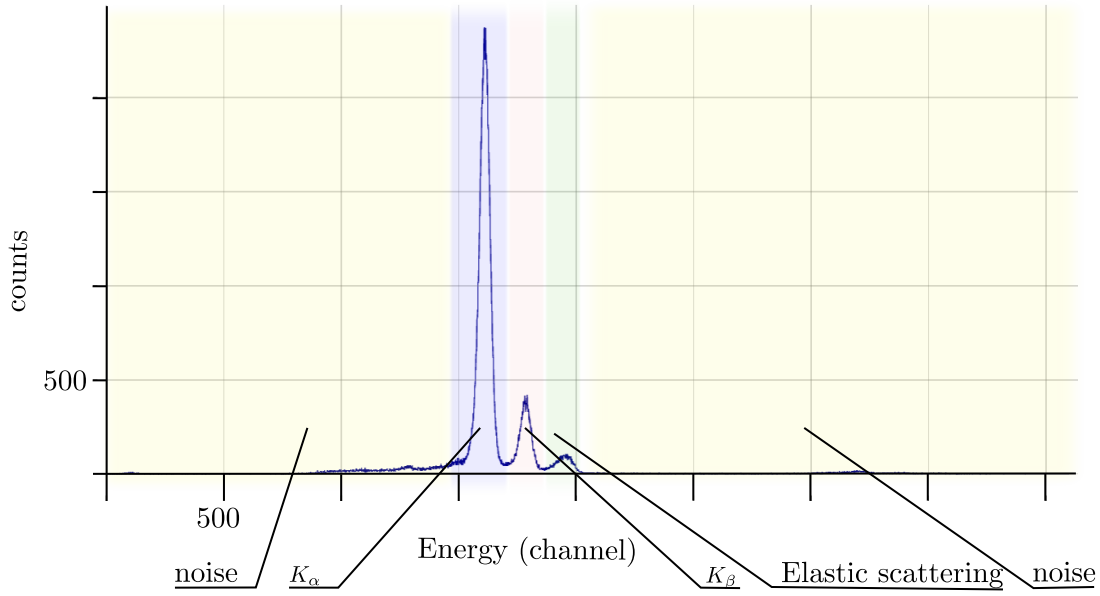

Figure 3.10: *Different regions of the fluorescence spectrum for the copper at a incident energy above the K edge*

To avoid information overload, the fluorescence spectra are deleted, retaining only the respective integral values. Another issue to be considered, is the pile-up inspection. As a matter of fact, the use of third-generation radiation sources provides extremely intense energy fluxes on the sample. Consequently, systematic pile-up effects cannot be neglected during the study of the detected photon counting. The dead-time correction method currently used at the LISA Beamline follows the following logic [3].

Starting from equation 3.5, the system throughput $\exp(-n\tau)$ can be experimentally determined by measuring the energy-integrated counting rates $n_T(E)$ and $m_T(E)$ using the two channels of the amplifier at each energy of the scan,

$$\exp(-n\tau) = \frac{m_T(E)}{n_T(E)} = \frac{1}{C(E)} \tag{3.6}$$

If we assume that the dead time of the fast channel in measuring the energy-integrated counting rate is negligible and that the correction factor $C(E)$ obtained from the energy-integrated counting rate is applicable to any subset of photons (independent of photon energy), then the true counting rate in the region of interest for each energy will be:

$$n_F(E) = m_F(E)C(E) \tag{3.7}$$

Where $n_F(E)$ and $m_F(E)$ differ from $n_T(E)$ and $m_T(E)$, as they refer to the counting rate in the region of interest of the pre-selected fluorescence line. Thus, by plotting the normalized and dead-time corrected fluorescence intensity against the respective source energy, we obtain a trend similar to figure 1.5. The inherent problem with this analysis method is that it is not possible to correct the region of interest for integrating the fluorescence signal once data acquisition has been completed. In other words, if we want to change the region of interest after the acquisition process has ended, for example, due to an unexpected event, it is simply not possible. Solving such a problem is the idea that lies at the roots of my project.

3.2 Structure of Developed Software Tools

The developed codes offer methods for investigating in the field of X-ray absorption fine structure analysis by fluorescence. In particular, two codes were created, each with a specific purpose. The first software, DataNexusConverter [7], aims to organize the data collected in a typical fluorescence experiment into the NeXus data format. The second software, ROIMaster [8], allows for reading the data previously collected in this format and enables important a posteriori analyses. Both codes are written in Python and can be found in my open GitHub repository at the following reference [24]. The aim of this paragraph is to describe the main purposes of the codes and how those programs work. DataNexusConverter is designed to streamline the conversion of experimental data into the NeXus data format [1], which is a standardized format used in neutron, X-ray, and muon science to facilitate data sharing and analysis. The software begins by accepting raw data files generated from fluorescence experiments. It then processes this data to conform to NeXus standards, incorporating appropriate metadata and ensuring the data is structured correctly. The output is a `.nx5` file, ready for further analysis and compatible with a wide range of analytical tools.

ROIMaster is intended for reading and analyzing data that has been organized into the NeXus format. In particular, when conducting a fluorescence experiment aimed at measuring the EXAFS signal of a specific chemical element at a specific energy threshold, the intensity value of the measured fluorescence peak is estimated by summing the number of counts within a certain integration domain (the Region of Interest). This method excludes counts of other physical origins, such as those due to the Compton effect or other fluorescence lines. At the LISA Beamline, the data acquisition and processing programs require specifying the integration region before acquiring the fluorescence signals, using pre-tabulated intervals. As a result, after data acquisition (as extensively explained in paragraph 3.1.4), the full spectra are typically deleted, and only the intensity values of the fluorescence peaks are stored. However, it may be useful to perform this integration process after acquiring the fluorescence spectra. The purpose of ROIMaster is exactly to permit this type of post-analysis.

3.2.1 DataNexusConverter

The code in question, as introduced above, allows for the storage of raw data from a fluorescence experiment into a NeXus data format. Before focusing on the core of the code, let's provide a general overview of how such a file is structured. NeXus defines a format that can serve as a container for all relevant data associated with a scientific instrument or beamline. There are four fundamental entities associated with these types of files: groups, fields, attributes, and links.

- *Groups* are like folders that can contain a number of fields and/or other groups.
- *Fields* can be scalar values or multidimensional arrays of a variety of sizes (1-byte, 2-byte, 4-byte, 8-byte) and types (characters, integers, floats). Fields are represented as HDF5 datasets [14].

- *Attributes* give extra information required to describe a particular group or field, such as the data units, can be stored as a data attribute. Attributes can also be given at the file level of an HDF5 file.[1]

- *Links* are used to represent the same information in different places.

In order to understand the work carried out by the tool, let's do a practical example of file.

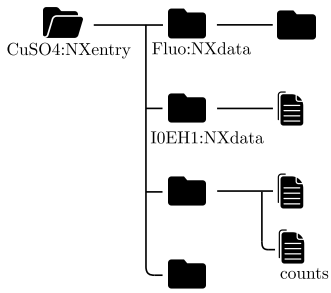

The tree structure of a NeXus file follows a typical hierarchical format. This system is designed to organize large volumes of experimental data in a simple and clear manner, similar to the example shown on the left. Folders represent the groups, and each group is identified by both a name and a class type.

Groups can contain other groups (subgroups) and fields, allowing for a nested, organized structure that reflects the relationships and dependencies within the data. On the left, sheets of paper represent the fields and they may store both experimental results (counts, icr, ocr etc.), and other information associated with the experiment (start and end times, user names, etc.). Fields are identified by their names, which must be unique within the group in which they are stored. The top level of any NeXus file contains one or more groups with the class NXentry. These contain all the data that is required to describe an experimental run or scan. There are several type of classes but those of our interest are the following:

- *NXdata*: This group contains the experimental results in a self-contained manner, meaning each NXdata group has all the necessary information to generate a meaningful plot of the data.

- *NXsample*: This group stores information about the sample, including its chemical composition, mass, and environmental conditions.

- *NXinstrument*: This group encompasses all relevant instrumental details for a measurement, such as flight paths, collimation, and chopper frequencies.

Attributes are extra (meta-)information that are associated with particular groups or fields. They are used to annotate data, e.g. with physical units or calibration offsets, and may be scalar numbers or character strings. In addition, NeXus uses attributes to identify plottable data and their axes, etc. In a tree structure, an attribute is usually shown with a @ prefix, such as `@units`. Finally, links act as pointers to data located elsewhere, similar to symbolic links in a Unix file system. The NeXus format often requires accessing the same data from multiple groups within the same file, and in order to do not replicate

[1]HDF5 is a scientific file format designed to store data from experiments of big dimensions. HDF5 can store two primary types of objects: datasets and groups.

the data, we use links. When the application is launched, the user interface appears as shown in figure 3.11. This interface is designed to guide the user step-by-step through the process of converting their files into the Nexus format. The "Load Config" button allows users to load the energy configuration of their experimental setup and is fundamental for configuring the energy scale associated with the experiment in question. Indeed, as widely discussed in paragraph 2.2, the monochromator uses a crystal to select the desired wavelength of the source radiation and the selection is performed through the crystal rotation at a specific Bragg angle.

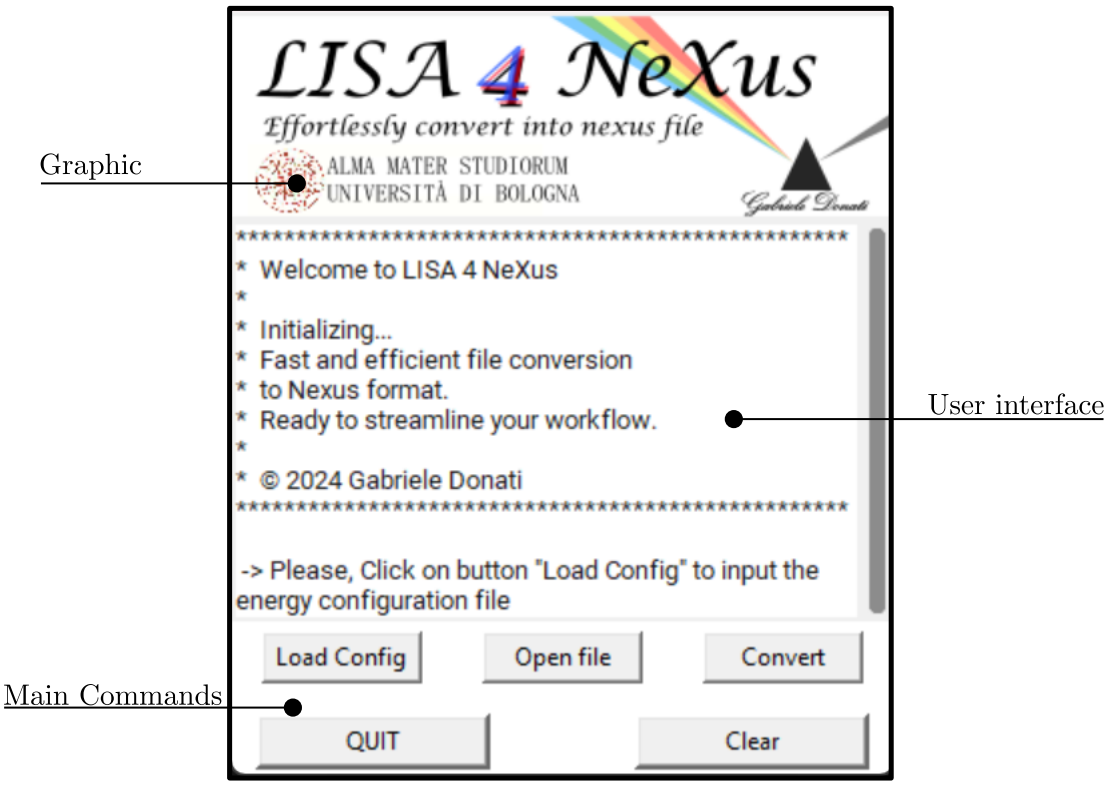

Figure 3.11: Graphical user interface of the into nexus file converter

The monochromator is motorized, and the rotational angle is controlled by an *encoder* that translates the rotation of the motor into steps. Nevertheless, the encoder is subject to a systematic error, which results in a offset between the theoretical angle predicted by the Bragg equation (Eq. 2.13) and the actual angle of rotation. The corrected energy is computed using the formula:

$$E_{\text{corr}} = \frac{f}{a_0 \sin\left(\frac{\varphi_{\text{Bragg}}+\Delta\varphi}{800000}\right)} \tag{3.8}$$

where $\Delta\varphi = \varphi_{\text{th}} - \varphi_{\text{exp}}$ is the difference between the theoretical angle and the experimentally measured angle (in the energy configuration file) at the edge point of the element, both measured as steps of the encoder. The factor f can assume three different values and depends on the planes of the monochromator used during acquisition, and a_0 is a fixed scale factor. The φ_{Bragg} are the encoder's steps experimentally measured. Once the energy configuration is completed, users proceed by opening the files they want to convert into the Nexus format. This is done through the file selection options provided in the interface. The application will then use the loaded energy configuration to correctly interpret and convert the data into the desired Nexus format, ensuring that all relevant experimental details are accurately captured and represented in the converted files. Furthermore, the code permits more than one conversion simultaneously. Let's consider an example of a NeXus file created with this tool. The file in question pertains to the experiment conducted at the Lisa Beamline with the objective of validating the developed software (further details are discussed in the next paragraph). At the top level of the file, there is the mandatory group belonging to the class NXentry. Within this group, additional nested groups are present. In particular, the "Fluorescence" folder is of the NXdata class type and contains the "Counts" field. There are typically multiple fluorescence folders, each corresponding to the fluorescence spectrum detected by different elements of the detector (typically 12). Within the top group, there are several sub-groups, such as I0EH1 and I0EH2, which contain the intensity values incoming against the sample in the two different experimental rooms, respectively. Another example is I1EH2, representing the intensity of the beam just after the sample in the EH2 experimental room. More important is the Instrument subgroup, which, unlike the others, belongs to the NXinstrument class. It is customary to include all experimental data obtained during the experiment within this group. The instrument subgroup contains other sub-groups related to the raw experimental data. The number of fluorescence groups automatically depends on the number of detector elements. Each element reports the fluorescence spectra, accompanied by the Input Count Rate (ICR) and Output Count Rate (OCR).

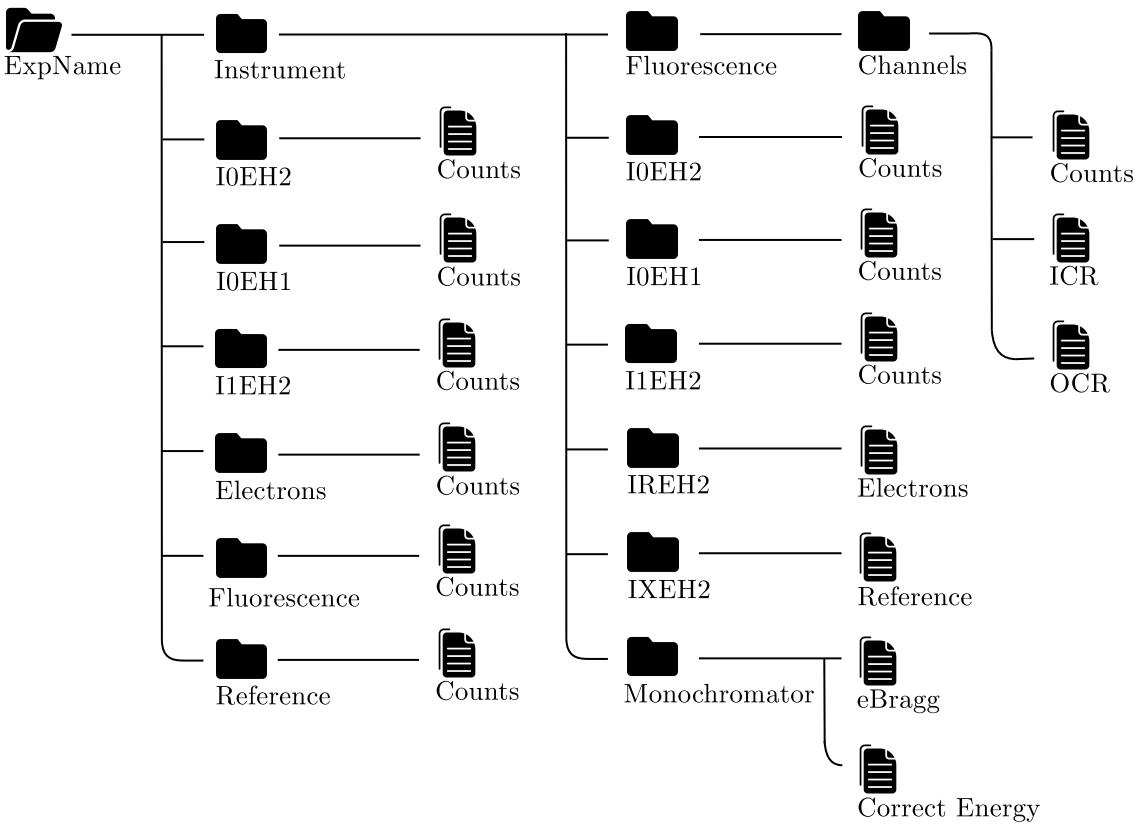

Figure 3.12: *Structure of the NeXus file which contains the data of the experiment aimed at validating this code*

Further explanations regarding the nature of these data are provided in the paragraph 3.1.3. Let's now delve into the technical structure of the code. This code is a Python script that creates a Graphical User Interface (GUI) application and the library imported are:

- **os**: Provides various functions to read or write a file or to manipulate paths.[18]
- **tkinter**: Standard GUI library in Python that provides a robust and platform independent windowing toolkit.[12]
- **ttk**: this module provides access to the `tkinter` themed widget set, introduced in `tkinter` 8.5.[28]
- **filedialog**: it contains convenience classes and functions for creating simple modal dialogs to get a value from the user.[27]
- **importlib.machinery**: used to load configuration files dynamically.[16]

- **numpy**: is the fundamental package for scientific computing in Python and provides a multidimensional array object and an assortment of routines for fast operations on arrays, including mathematical, logical, shape manipulation, sorting, selecting, I/O, discrete Fourier transforms, basic linear algebra, basic statistical operations, random simulation and much more.[19]

- **PIL (Pillow)**: this library provides extensive file format support, an efficient internal representation, and fairly powerful image processing capabilities.[21]

The main user-defined functions aim to carry out the features described above. Here is a brief explanation of these functions:

- `loadConfig()`: It is designed to load the energy configuration file. The input file must be a `.txt` file to ensure the correct functioning of the code. It extracts three pieces of information from the file (The element in the sample being studied, the specific absorption edge of this element, and the experimental reading from the encoder at the corresponding energy level), which are fundamental during the conversion process.

- `convertFile()`: The function reads data from specified `.dat` files, performs necessary calculations and data manipulations, and writes the results into new `.nx5` files, structured according to the NeXus format. Specifically, the energy counts are first corrected using an equation, with correction values extrapolated by the `loadConfig()` function. Furthermore, a tree data structure is created and populated with experimental data as described above. Links are created between datasets and groups to ensure the data is accessible in a structured manner. The output file name is derived from the input file's name by adding the extension `.nx5`.

3.2.2 ROIMaster

The core of my project involves developing an application that enables the type of post-analysis described in the introduction of this paragraph (3.2). What might seem like a simple programming exercise actually hides a complex problem to solve, and there are several interesting points to analyze. Since the fluorescence spectra analyzed by the application are those collected through the slow filter in the measurement process (see 3.1.2), they are not corrected for dead time (Paragraph 3.1.4). This means that the program's work does not consist of merely integrating spectra but also necessarily correcting the experimental results obtained. In Fig. 3.13, the graphical interface of the application upon startup is depicted. First, the "Open File" button allows you to load the `.nx5` file you wish to analyze. Once the file is loaded, a table will appear containing all the fluorescence spectra, one for each detector element and energy. By clicking on a spectrum, it will be plotted on the Cartesian graph at the bottom right (initially blank), at the energy specified by the slider. Here, the region of interest for integrating the fluorescence spectrum can be selected, by simply using the mouse. In real-time, the corresponding EXAFS signal computed from the selected region of interest will appear at the top right.

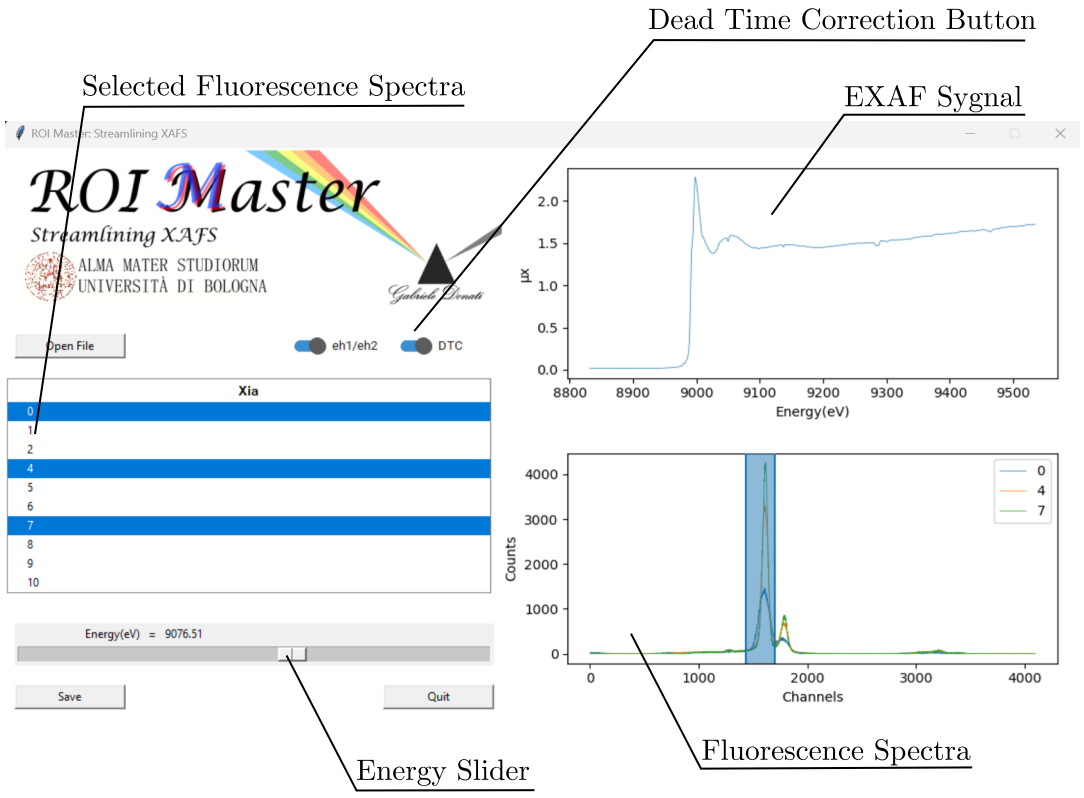

Figure 3.13: *Graphical user interface of the ROIMaster application*

There are also two important buttons that need to be mentioned: the "DTC" button and the "eh1/eh2" button. The "DTC" button allows you to perform a dead-time correction on the EXAFS signal that has just been computed. Specifically, the code performs the following steps: it extracts the fluorescence photon count rates detected by the slower filter (OCR) and the faster filter (ICR) for each energy value in the scan. It then calculates the ratio between these two values for each energy point and multiplies this ratio by the integrated intensity of the fluorescence spectrum within the region of interest. The "eh1/eh2" button lets you select which normalization data to use, between the radiation intensity recorded in the EH1 room or EH2.

It is important to note also that more than one spectrum can be selected simultaneously. In the bottom right graph, they appear overlapping in different colors, and the EXAFS signal is computed by summing all the different selected spectra (within the same selected region).

In order to better understand the functioning of the program, let's analyze the developed code. The code starts with the importation of the libraries used, most of which have already been mentioned before. Among these, the following libraries are notable:

- **h5py**: This library allows for the storage of large amounts of numerical data and makes it easy to manipulate that data using `NumPy`.[13].

- **pandas**: It is an open source library providing high-performance, easy-to-use data structures and data analysis tools [20]

- **ast**: This module helps Python applications to process trees of the Python abstract syntax grammar.[4]

Moreover, to facilitate the organization and manipulation of fluorescence spectra, the class `DataFluo` has been developed. This class contains all the crucial information needed for the correct functioning of the code and the accurate description of the data. The class in question aims to codify the data stored in the NeXus file. The attributes of the class are:

- **energy**: an array that contains the correct value of the scan energy. These data are extracted from the NeXus file from the following NeXus path: "ExpName/Instrument/Monochromator/Correct Energy". (See Fig. 3.12)

- **name**: a string that represents the name of the detector element that has performed the data acquisition (e.g., fluo06).

- **ixeh2**, **i1eh2**, **i0eh2**, **i0eh1**: photon and electron count rates associated with the respective detectors.

- **spectra**: a Python dictionary [23] that stores the fluorescence spectra for each detector element. The keys are the names (labelled by a number) of the detector elements and the values are the respective spectral data.

- **correction**: a Python dictionary that contains the correction data for each detector element. The keys are the names of the detector elements, and the values are extracted by the ratio between the input count rate and the output count rate. These data are stored within the NeXus file at the respective paths: ExpName/Instrument/Fluorescence/channels/ICR and ExpName/Instrument/Fluorescence/channels/OCR.

- **metadata**: a Python dictionary that contains the metadata related to the respective fluorescence spectra. The keys are "crystal" and "time," and the values are those extracted from the attributes of the monochromator and entry class.

- **channels**: It is an array that contains the intensity values for all 4096 channels of the detector. Each channel represents the intensity of the detected fluorescence photons.

Let's now consider the main user-defined functions developed that permit to manipulate the data.

- `open_file()`: It is designed to open a NeXus file of the type described above, extract the stored data, and organize these into a `DataFluo` object.

- `plot_fluo()`: This function is designed to plot fluorescence data on a canvas within a Grafical User Interface. In particular, the fluorescence data for the selected energy is extracted from the `.spectra` attribute and plotted versus the channel data taken from `.channel` attribute.

- `plot_exafs()`: This function aims to plot the EXAFS signal. It calculates the integral of the fluorescence spectrum within the specified channels range, optionally applying a correction if "DTC" is on, and normalizes it by either `.i0eh2` or `.i0eh1` attribute. If multiple elements are selected, it sums the integrals of the spectra from all selected elements, again optionally applying the correction. The integrated and normalized data is then converted to a `pandas` DataFrame. The function plots the energy versus the integrated intensity, setting the x-axis label to "Energy(eV)" and the y-axis label to μx.

- `save()`: It permits saving the EXAFS data with a `.xdi` extension. Specifically, a Python list containing the following data is initialized: energy values rounded to the second decimal place, incoming beam intensity `.i0eh2` or `.i0eh1` depending on the button's value, and the integrated and normalized fluorescence data (the effective EXAFS signal). Furthermore, the user-defined function creates a new file with a name derived from the `.name` attribute and writes metadata and data to it. Listing 3.1 is an example of the created file.

```
# XDI/1.0 GSE/1.0
# Scan-start_time: 2024-06-25T11:31:21
# Column.1: energy (eV)
# Column.2: I0
# Column.3: Fluo
# Column.4: I1
# Column.5: IR
# Mono.name: Si 111
# Mono.d_spacing: 3.134692
# Mono.notes: LNT cooled
# Beamline.name: BM08-LISA
# Facility.name: ESRF
# Facility.xray_source: Bending magnet
# DTC: True
# Norm: eh2
# Xmin: 1495
# Xmax: 1709
# energy eV I0 Fluo I1 IR
8832.26 611828 0.004911828566580978 2634486 2597900
8837.08 611938 0.0048684670669250805 2634485 2605478
8841.98 612104 0.0047749602636606246 2634486 2613990
.       .
.       .
.       .
```

Listing 3.1: Example of a .xdi file created by the application

3.3 Validation of Developed Software Tools

In order to check the applicability of the post-correction methods presented above and the operation of the developed software, two test experiments has been performed at the LISA Beamline of the European Synchrotron Radiation Facility in Grenoble, France.

3.3.1 First Validation

The first experiment carried out aims to check the validity of the dead time correction method explained in paragraph 3.1.4. The sample analyzed was copper sulfate ($CuSO_4$), sprinkled in a cellulose matrix with a mass percentage of 1.6%. The filling mode of the storage ring was 16 bunch, with a current of 75 mA. In this context, using this sample at this concentration level has the advantage of producing an intense Cu K_α fluorescence line. This ensures that the non-linearity effect will be significant, making it highly suitable for studying dead time correction. Moreover, the spectrum of photons emitted from the sample will be dominated by this fluorescence line with negligible contribution from elastic or Compton scattering. The detector used was a 12-element high-purity germanium model (ORTEC) and the pulse-processing electronics was a Digital X-ray Processor(DXP) (model XMAP) manufactored by XIA, sets in Multi-Channel Analyzer (MCA) mode. In this sampling mode, a data acquisition run produces a single energy spectrum (2048 bins) and associated run statistics for each processing channel. The memory is normally cleared at the beginning of a run. This electronics has trapezoidal fast and a slow amplifier channels which run at the same time (see paragraph 3.1.4) and each detector element is coupled to an independent pulse-processing electrons channel. As a first step, the system's throughput was determined at a fixed incoming photons energy (9 keV) by measuring the fluorescence count rate in the slow amplifier channel as a function of the integrated count rate recorded in the fast channel. This was accomplished by gradually opening the slits to vary the intensity of the beam hitting the sample. The system throughput was fitted with the following equation:

$$n = am\exp(-\tau m) \tag{3.9}$$

Where a and τ are free parameters. Parameter a takes into account that the variable m, which represents the fast channel count rate, is minimally influenced by dead time despite being recorded through the fast channel. Parameter τ represents obviously the dead time. The result is shown in figure 3.14. The fit gave $a = (0,997 \pm 0,001)$ and $\tau = (2,170 \pm 0,007)\mu s$, in reasonable agreement with the expected values. The reduced Chi-square of the fit is $\chi^2_{red} = 0,91$ and this implies that the dead time model suggested in 3.1.4 is effective for studying this phenomenon. In order to directly verify the compactness of the time correction model proposed in paragraph 3.1.4, we want to check the effective corrections experimentally obtained. In particular, using a Python script, the counts around the Cu K_α line in the fluorescence spectrum of copper sulfate (in other words the spectrum achieved by the slow channel) was summed a posteriori. This allows to calculate the emission intensity of that specific fluorescence line affected by dead-time pill-up. Subsequently, the dead time correction proposed in paragraph 3.1.4 is applied.

We repeated this procedure for each slits aperture configuration and then plotted the integral against the incident intensity (linearly proportional to the slits opening). Finally, we verified that the fit was indeed linear, thus validating the proposed correction. In figure 3.15 are compared the results of the below analysis. Another important proof of the consistency of the post-correction method is the comparison between these data corrected *a posteriori*, and the statistics extracted by SPEC routines on the LISA Beamline in real-time. The routines in question provide a deadtime correction extensively described in the article *Treatment of EXAFS data taken in the fluorescence mode in non-linear condition* [3]. Briefly, the method in question is referred to as *method II* in the aforementioned article and is applied in real-time during data acquisition. Assuming this method is valid, we expect that for each slits opening, the difference between the data post-corrected and the data corrected with method II is roughly zero. Figure 3.16 represents the difference and the fit with the straight line $y = ax + b$ within the domain $0.2 - 1.4$ V. The results of the fit give $a = (0.7 \pm 0.5)(\text{Vs})^{-1}$ and $b = (-0.6 \pm 0.4)\ \text{s}^{-1}$. We note that the constant line $y = 0$ falls within the experimental uncertainty ranges, suggesting that the results are satisfactory. From a quantitative point of view, performing the p-value test with the null hypothesis that the experimental values follow a null path, we obtain a high probability that the offset is due to chance. Indeed, the p-value of the fit with the null constant is $p_n = 0.59$, confirming the consistency of the post-correction method with 95% of probability.

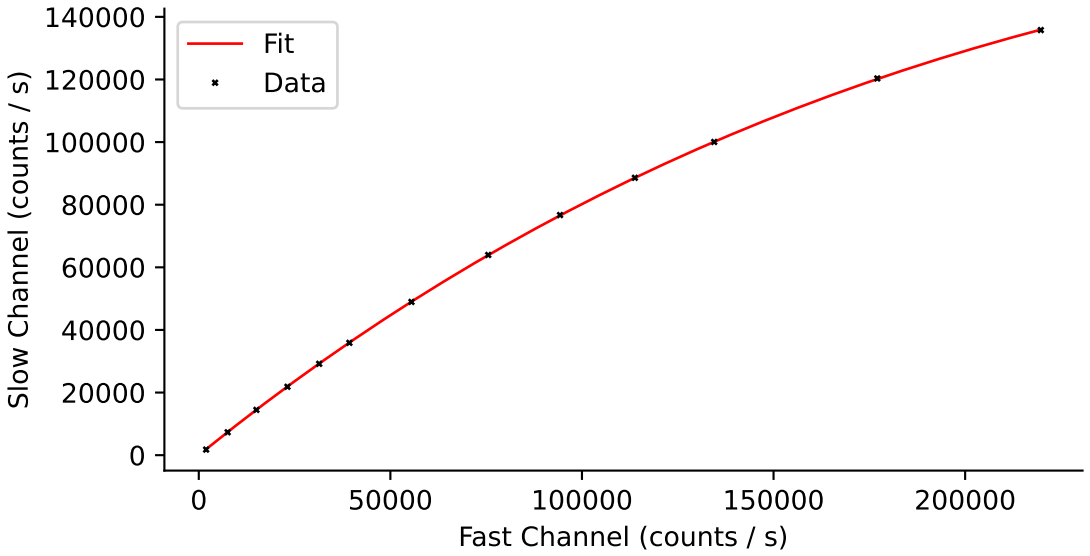

Figure 3.14: *Slow channel counts versus fast channel counts Each dot represents a different slit opening. The red line represents the best fit of the data. This plot is referred to channel 6 of the detector.*

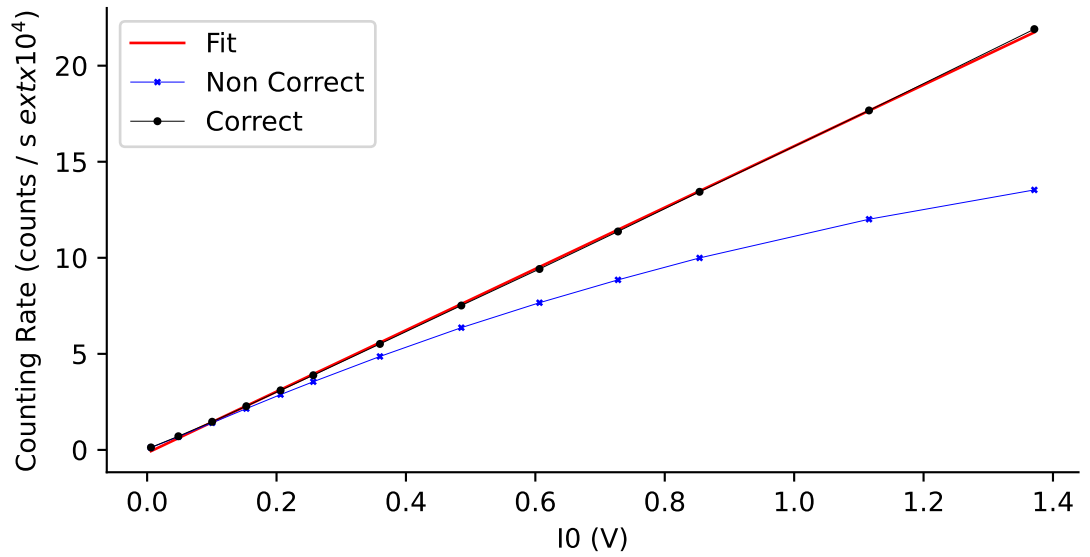

Figure 3.15: *Comparison between corrected and uncorrected data with linear fit, related with the channel 6 of the detector. The graph overlays corrected data (black line) and uncorrected data (blue line) for direct comparison as incident intensity increases. . The red line represents the linear fit applied to the corrected data, highlighting a significant relationship between corrected and uncorrected emission intensities.*

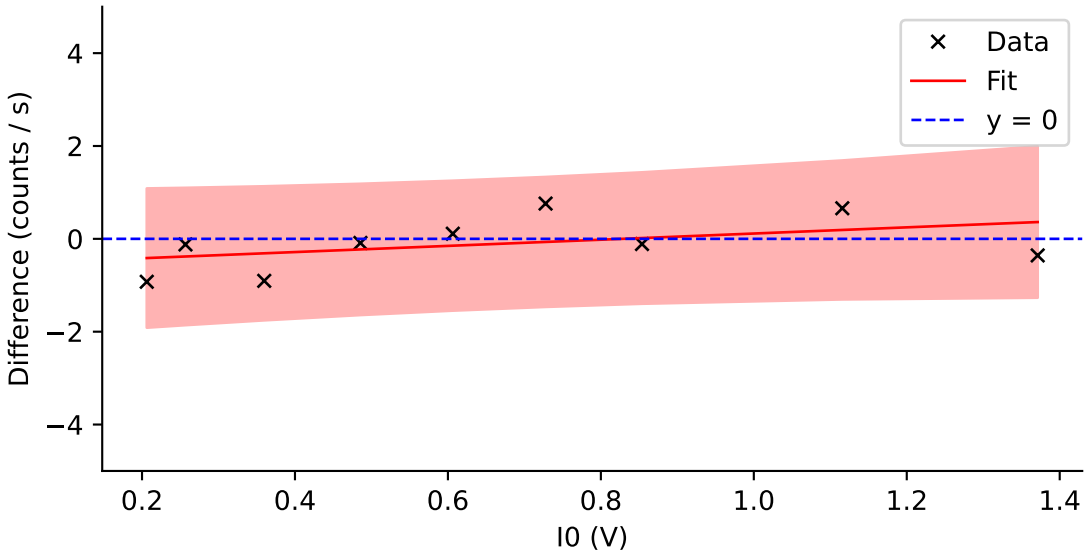

Figure 3.16: *The plot shows the difference between the data post-corrected using the proposed method and the data corrected in real-time using method II. The solid line represents the best fit while the blue dashed line represents the expected trend. The shaded region around the line corresponds to the* 95% *confidence interval, showing the range where the true values of* y *are expected to lie with* 95% *confidence.*

3.3.2 Second Validation

The second experiment consists of a fluorescence experiment conducted to verify the effective functioning of the second software tool described in Section 3.2.2. In particular, five energy scan collections were conducted by gradually opening the slits to vary the intensity of the incoming beam, in such a way the dead time distortion is highlighted especially for high intensity. We want to verify that the EXAFS signal, extracted from fluorescence and subsequently corrected for dead time as proposed previously, remains reliable even at high count rates. The experimental setup is similar to that described in the previous experiment. The sample analyzed was copper sulfate once more, and therefore the same properties are valid. We performed an energy scan by varying the angle of the monochromator, covering an energy range from 8830 eV to 9840 eV. This range ensures that we will observe the K-edge of copper. Additionally, a SPEC data acquisition routine which allows for the saving of 12 complete fluorescence spectra of copper, one for each detector element, has been developed. This routine is designed to acquire and store all spectral data without requiring the pre-definition of the region of interest (ROI). Consequently, as depicted in figure 3.17, it is possible to analyze and select the region of interest later, during the data processing phase, rather than having to specify it before acquisition. By adjusting the region of interest depending on which channel we want to analyze, it is possible to extract the preferable EXAFS signal.

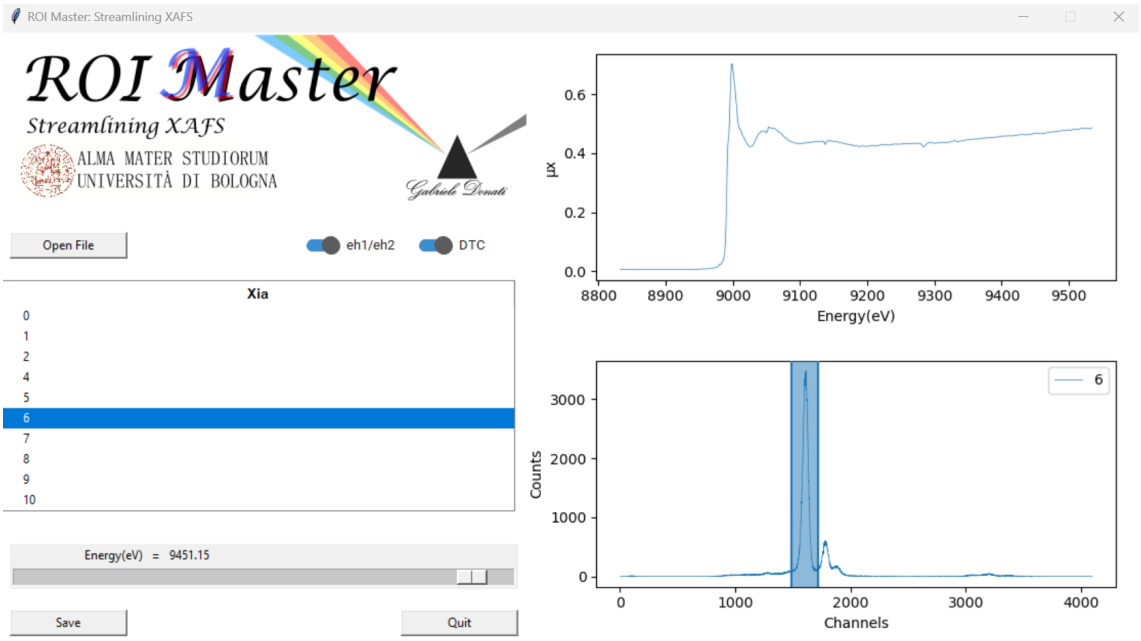

Figure 3.17: *The graph in the bottom right represents the complete fluorescence spectrum for channel 6, with the region of interest highlighted in blue. The EXAFS function, shown in the top right, is computed starting from this specified region of interest.*

As depicted in figure 3.18, adjusting the region of interest allows for the analysis of

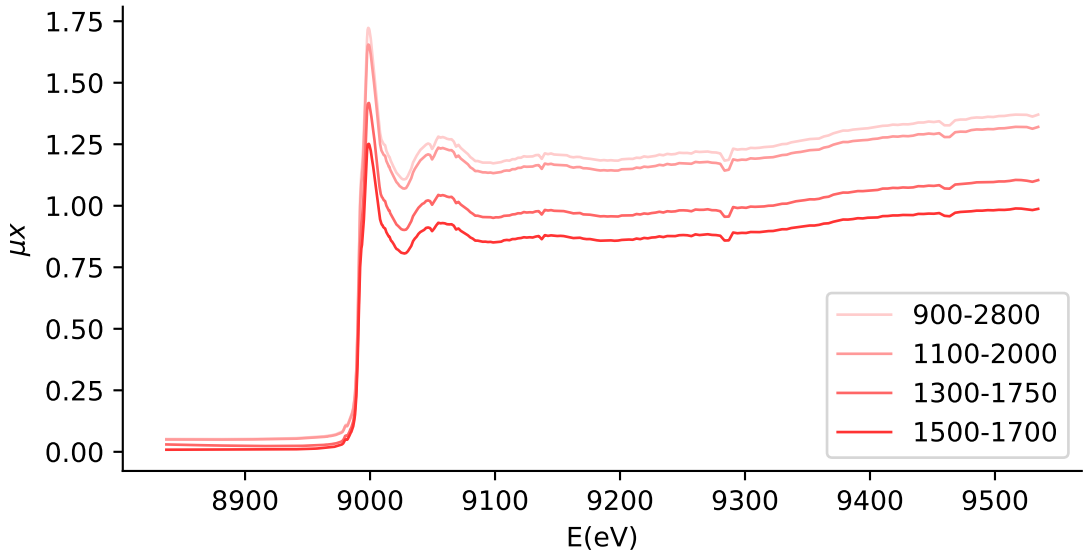

Figure 3.18: *The EXAFS signal demonstrates variation when different a posteriori-selected regions of interest (ROIs) are employed. The data have been corrected for deadtime.*

different EXAFS signals. Notably, focusing closely on the K_α peak, in the fluorescence spectrum, can lead to a improve in the observed EXAFS signal. This enhancement is primarily due to the overlap of the K_α with other spectral features such as the Compton peak and background signals from K_β fluorescence. The Compton peak, resulting from inelastic scattering, and the K_β emission line, arising from higher energy X-ray fluorescence, can both affect the measurement and interpretation of the absorption edge.

The following table summarizes the count rate values as the region of interest in which the events are counted is reduced. The results refer to an energy of 9 keV and a slits opening of $ehg = 12mm$. The experimental uncertainty has been computed by taking into account that each detector channel is affected by Poissonian noise.

Counts for different ROI	
Region of Interest (channel)	*Counts / s* $\times 10^6$
900 - 2800	1.300 ± 0.001
1100 - 2000	1.250 ± 0.001
1300 - 1750	1.070 ± 0.001
1500 - 1700	0.950 ± 0.001

Now, we want to evaluate how the dead-time distort the data in a quantitative way. Taking into account the nomenclature presented in figure 3.19, we will use the letter w to represent the *white line*, that is the height of the EXAFS signal at the energy peak E_0, and the letter j to represent the height calculated at the energy peak E_0 of a quadratic polynomial fit over the range from 8950 to 9500 eV, named *jump*. The fit has been developed by Athena (XAS Data Processing)[5]. We are particularly interested in studying the ratio between w and j as the slits open. As the slits in the experimental setup are gradually opened wider, the deadtime distortion becomes increasingly pronounced. Consequently, as the slits are opened more, this distortion leads to a noticeable reduction in the peak value of the recorded signal. This decrease is particularly evident when deadtime corrections are not applied to the data.

The consequences of dead time correction				
ehg	*w(dtc)*	*j(dtc)*	*w(no dtc)*	*j(no dtc)*
3	0.504 ± 0.003	0.324 ± 0.003	0.412 ± 0.001	0.281 ± 0.001
6	0.687 ± 0.003	0.462 ± 0.003	0.437 ± 0.001	0.337 ± 0.001
9	0.900 ± 0.004	0.596 ± 0.004	0.491 ± 0.001	0.383 ± 0.001
12	1.228 ± 0.004	0.758 ± 0.004	0.428 ± 0.001	0.414 ± 0.001
15	1.241 ± 0.005	0.871 ± 0.005	0.402 ± 0.001	0.409 ± 0.001

Table 3.1: *The table shows the effects of dead time correction on the white line and the jump in the EXAFS signal for copper as the slit openings increase.*

The uncertainties calculation is explained in Appendix A. To better understand and quantify the impact of deadtime distortion, we compare the ratios of the signal peaks with and without deadtime corrections: Plotting the ratios (Fig. 3.20), we can visualize how

The ratios		
ehg	*w/j (dtc)*	*w/j(no dtc)*
3	1.56 ± 0.12	1.46 ± 0.08
6	1.50 ± 0.10	1.29 ± 0.06
9	1.50 ± 0.10	1.29 ± 0.06
12	1.62 ± 0.10	1.05 ± 0.05
15	1.42 ± 0.09	0.98 ± 0.05

Table 3.2: *The table shows the ratios of w/j with and without dead time correction for different ehg values.*

effective the post-deadtime correction is in adjusting for the inaccuracies introduced by the deadtime effect. This comparison provides valuable insights into the extent to which the correction process compensates for the distortion. From the analysis, it becomes clear that as the slits are opened further, the need for deadtime correction grows more significant. This is because the wider slits increase the likelihood of overlapping signals and extended processing times, amplifying the deadtime distortion. Indeed, by fitting a linear regression ($y = ax+b$) to the uncorrected experimental data, we obtained a negative slope, indicating that the white line is decreasing rapidly. The fit results are as follows: $a = (-0.040 \pm 0.006)\,\mathrm{mm}^{-1}$ and $b = (1.57 \pm 0.06)$. Despite this growing need for correction, the data corrected for deadtime shows a pattern that aligns closely with expectations. Specifically, the corrected data exhibit a linear behavior, which supports the predictions about how the system should ideally respond under these conditions. As a matter of fact, by fitting the corrected data with a linear function, we obtain $a = (-0.005 \pm 0.009) mm^{-1}$ and $b = (1.57 \pm 0.09)$, in other hands, the slope parameter a is an order of magnitude smaller than that of the non-corrected data. Another critical aspect of our analysis involves comparing the EXAFS signal extracted using the ROIMaster application with the signal obtained in real-time using the existing SPEC routine during the data acquisition process. The SPEC routine is designed to perform real-time corrections on the fluorescence spectrum as the data is being collected. This real-time correction aims to account for various distortions and artifacts that may occur during acquisition, such as background noise and deadtime effects. However, this approach has the potential drawback of extending the overall acquisition time, as the system must continuously process and correct the data on-the-fly. Additionally, real-time corrections can introduce their own sources of noise and inaccuracies, which may affect the quality of the final signal. In contrast, ROIMaster operates on a different principle. Instead of attempting to correct the data in real-time, ROIMaster performs all necessary corrections after the data collection phase is complete. This post-acquisition approach allows for a more thorough and precise adjustment of the data. By focusing on the quality of the collected signal without the added complexity and potential noise introduced during real-time correction, ROIMaster can reduce the impact of these artifacts and achieve a cleaner, more accurate signal. The results of our comparison (Fig. 3.21) indicate that the EXAFS signal extracted using ROIMaster is notably less noisy compared to the signal obtained with the SPEC routine. This difference is primarily attributed to the fact that post-acquisition corrections performed by ROIMaster can be optimized without the constraints and real-time processing overhead that affects the SPEC routine. By addressing noise and distortions after the data has been collected, ROIMaster minimizes the impact of correction-related noise, resulting in a clearer and more reliable EXAFS signal.

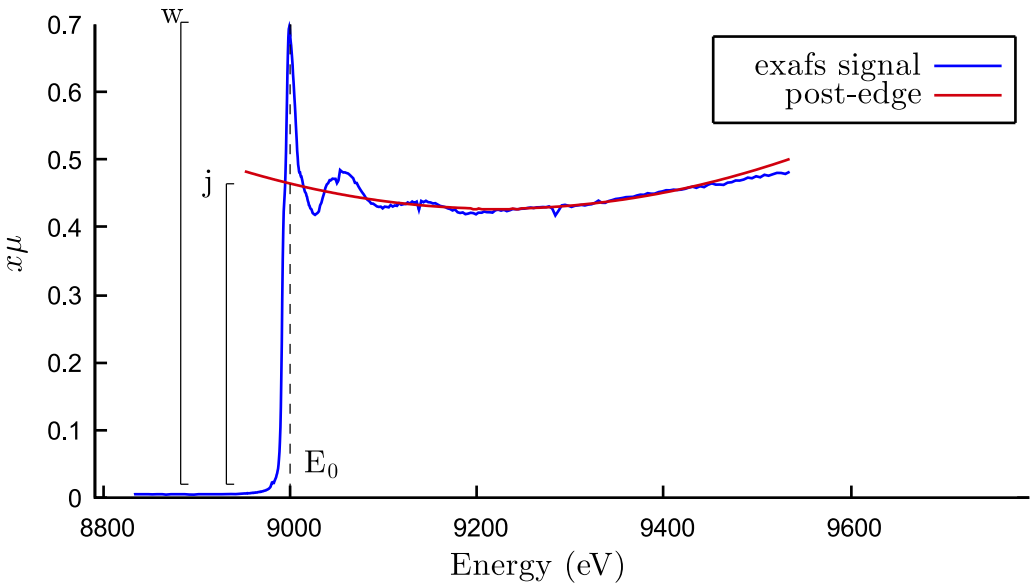

Figure 3.19: *The EXAFS signal with a post-edge fit was performed by Athena using a quadratic function with three free parameters in a limited domain range. The maximum of the signal, computed at E_0, is indicated by 'w'. The value of the fit function, always calculated at the same energy, is indicated by 'j'*

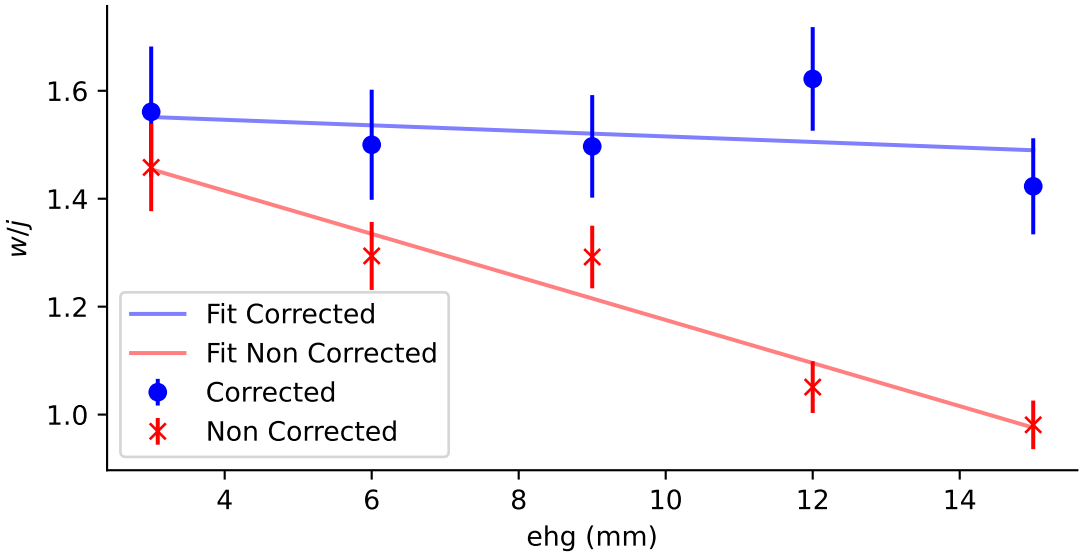

Figure 3.20: *Ratio between the maximum 'w' of the EXAFS signal, computed at E_0, and the value j' of the quadratic fit function calculated at the same energy. Each experimental point corresponds to a specific slit opening. Furthermore, both the corrected and non corrected data are compared with a linear fit to highlight the validity of the correction.*

3.3.3 Conclusion

In conclusion, we have demonstrated that the developed software tools are effective. Specifically, the first application facilitates the rapid conversion of data to an NeXus format file, which is then promptly processed by the second application, ROIMaster. The innovation of these tools lies in their ability to extract the EXAFS signal by defining the Region of Interest (ROI) after the data has been acquired. This approach allows for focusing on different areas of interest depending on the situation and helps avoid including counts that are not relevant to our objectives.

Furthermore, we have tested the program's ability to correct data affected by deadtime. This correction is crucial, especially at high count rates, to obtain physically reasonable results. As demonstrated in 3.3.2 and 3.3.1, even for high photon flux, post-correction analysis maintains the linearity between the intensity of the incoming radiation and the events effectively detected by the detectors (see Fig. 3.15), and prevents distortion of the EXAFS signal (see Fig. 3.20). This result is particularly significant as it shows that the corrected signal preserves proportionality, providing accurate results even under high-stress conditions, such as when studying materials with high fluorescence emission.

Additionally, since deadtime correction is applied post-acquisition, the data processing time is reduced, resulting in lower noise levels as depicted in Fig.3.21.

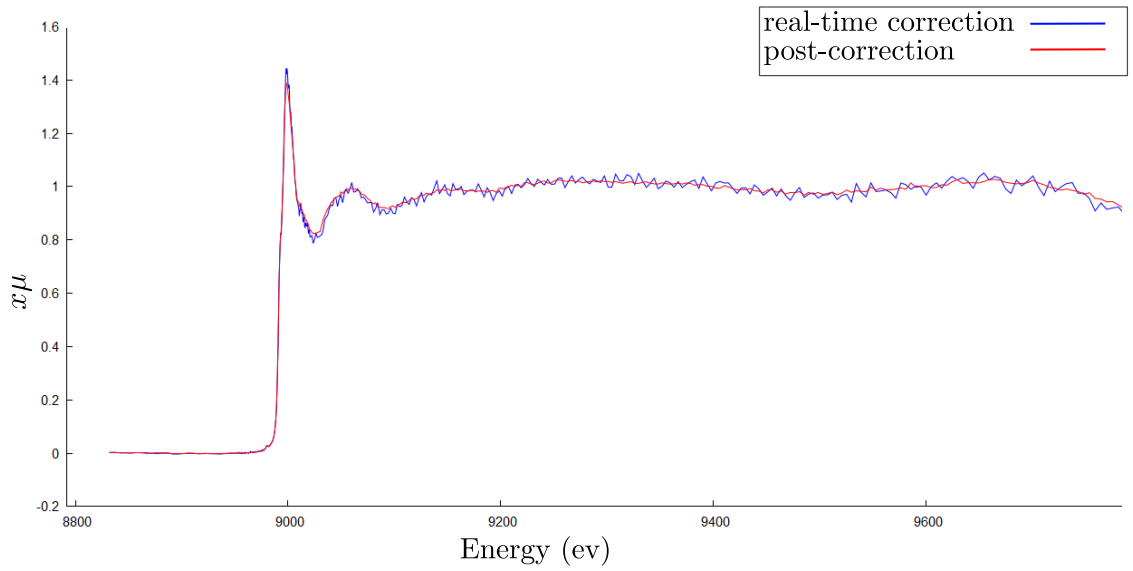

Figure 3.21: *EXAFS signals of copper (Cu) in $CuSO_4$ at K edge obtained using the fluorescence method are shown. Both signals are for element 6 of the detector. The blue graph represents the signal computed in real-time using existing SPEC routines, with a fixed region of integration set before the acquisition. The red graph represents the signal extracted by ROIMaster, using the same region of interest defined post-acquisition.*

A Uncertainties Calculation

In order to compute the experimental uncertainty of the white line w and the jump j appearing in the table 3.1, we have first to remember how these parameters are calculated. The developed code allows the following calculation:

$$\mu_c(E_0) = \frac{R}{I_0}\frac{I}{O} \tag{10}$$

where $\mu_c(E_0)$ is the deadtime corrected EXAFS signal calculated at its maximum at the source energy E_0. R is the intensity of the K_α peak within the selected region of interest (ROI) for the fluorescence spectrum at E_0. I and O represent the input and output count rates, respectively, for the spectrum at the source energy E_0.

According to general theory, for statistically uncorrelated measurements, the uncertainty of the measurement in Equation 10 is given by:

$$\delta\mu_C = \sqrt{\left(\frac{\partial\mu_c}{\partial R}\delta R\right)^2 + \left(\frac{\partial\mu_c}{\partial I}\delta I\right)^2 + \left(\frac{\partial\mu_c}{\partial I_0}\delta I_0\right)^2 + \left(\frac{\partial\mu_c}{\partial O}\delta O\right)^2} \tag{11}$$

Performing the calculations, we obtain:

$$\delta\mu_C = \sqrt{\left(\frac{I}{I_0 O}\delta R\right)^2 + \left(\frac{R}{I_0 O}\delta I\right)^2 + \left(\frac{RI}{I_0^2 O}\delta I_0\right)^2 + \left(\frac{RI}{I_0 O^2}\delta O\right)^2} \tag{12}$$

Since the uncertainty associated with the detector channels follows a Poisson distribution, the uncertainty of the quantities on the right side of Equation 10 can be approximated by the square root of the respective values. Hence it follows:

$$\delta\mu_C = \sqrt{\frac{I^2 R}{I_0^2 O^2} + \frac{R^2 I}{I_0^2 O^2} + \frac{R^2 I^2}{I_0^3 O^2} + \frac{R^2 I^2}{I_0^2 O^3}}. \tag{13}$$

Acting in the same way, we can estimate the experimental uncertainty for the non corrected EXAFS signal

$$\mu_{nc} = \frac{R}{I_0}. \tag{14}$$

In particular we obtain:

$$\delta\mu_{nc} = \sqrt{\frac{R}{I_0^2} + \frac{R^2}{I_0^3}} \tag{15}$$

Bibliography

[1] *About the NeXus Data Format*. URL: https://www.nexusformat.org/. (accessed: 21.07.2024).

[2] Francesco d'Acapito et al. "The LISA beamline at ESRF". In: *Journal of Synchrotron Radiation* 26 (2019). DOI: https://doi.org/10.1107/S160057751801843X.

[3] Gianluca Ciatto et al. "Treatment of EXAFS data taken in the fluorescence mode in non-linear conditions". In: *Journal of Synchrotron Radiation* 11 (2004), pp. 278–283.

[4] *ast — Abstract Syntax Trees*. URL: https://docs.python.org/3/library/ast.html. (accessed: 26.07.2024).

[5] *ATHENA: XAS Data Processing*. URL: https://bruceravel.github.io/demeter/documents/Athena/index.html#athena-xas-data-processing. (accessed: 20.07.2024).

[6] Vincenzo Barone. *Relatività, princìpi e applicazioni*. Bollati Boringhieri editore s.r.l, 2004. ISBN: 8833957578.

[7] Gabriele Donati. "DataNexusConverter". In: (2024). DOI: 10.5281/zenodo.12180834.

[8] Gabriele Donati. "ROIMaster: An Innovative XAFS Data Analysis Program". In: (2024). DOI: 10.5281/zenodo.12179398.

[9] Robert Martin Eisberg. *Quantum Physics of Atoms, Molecules, Solids, Nuclei, and Particles*. Hamilton Printing Company, 1985. ISBN: 047187373X.

[10] P. A. Lee P. H. Citrin P. Eisenberger and B. M. Kincaid. "Extended x-ray absorption fine structure—its strengths and limitations as a structural tool". In: *Reviews Of Modern Physics* 53.769 (1981). DOI: https://doi.org/10.1103/RevModPhys.53.769.

[11] EXAFS.HTML. *Principes de la spectroscopie EXAFS*. URL: https://www.esrf.fr/fr/home/UsersAndScience/Experiments/CRG/BM30/EXAFS.html.html. (accessed: 23.06.2024).

[12] *Graphical User Interfaces with Tk*. URL: https://docs.python.org/3/library/tk.html#graphical-user-interfaces-with-tk. (accessed: 24.07.2024).

[13] *HDF5 for Python*. URL: https://docs.h5py.org/en/stable/. (accessed: 26.07.2024).

[14] *HDF5, Hierarchical Data Format, Version 5*. URL: https://www.loc.gov/preservation/digital/formats/fdd/fdd000229.shtml#:~:text=Full%20name,of%20objects%3A%20datasets%20and%20groups.. (accessed: 22.07.2024).

[15] Albert Hofmann. *The Physics Of Synchrotron Radiation*. Cambridge University Press, 2007. ISBN: 9780521037532.

[16] *importlib — The implementation of import*. URL: https://docs.python.org/3/library/importlib.html. (accessed: 24.07.2024).

[17] *L'ESRF EN BREF*. URL: https://www.esrf.fr/fr/home/about/espace-presse/esrf-in-brief.html. (accessed: 23.06.2024).

[18] *Miscellaneous operating system interfaces*. URL: https://docs.python.org/3/library/os.html. (accessed: 24.07.2024).

[19] *NumPy documentation*. URL: https://numpy.org/doc/stable/. (accessed: 24.07.2024).

[20] *pandas documentation*. URL: https://pandas.pydata.org/docs/. (accessed: 26.07.2024).

[21] *Pillow*. URL: https://pillow.readthedocs.io/en/stable/. (accessed: 24.07.2024).

[22] Alessandro Puri. *LISA XAS Database*. DOI: 10.5281/zenodo.10778098. URL: https://lisa.iom.cnr.it/xasdb/. (accessed: 22.06.2024).

[23] *Python Dictionaries*. URL: https://www.w3schools.com/python/python_dictionaries.asp. (accessed: 26.07.2024).

[24] *ROIMaster-ESRF-LISA*. URL: https://github.com/GabriDona/ROIMaster-ESRF-LISA. (accessed: 22.07.2024).

[25] Bernhard Rupp. *X-ray Absorption Edge Energies*. URL: https://www.ruppweb.org/Xray/elements.html. (accessed: 22.06.2024).

[26] Carlo Meneghini Settimio Mobilio Federico Boscherini. *Synchrotron Radiation*. Springer-Verlag Berlin Heidelberg, 2015. ISBN: 978-3-642-55314-1. DOI: 10.1007/978-3-642-55315-8.

[27] *Tkinter Dialogs*. URL: https://docs.python.org/3/library/dialog.html. (accessed: 24.07.2024).

[28] *tkinter.ttk — Tk themed widgets*. URL: https://docs.python.org/3/library/tkinter.ttk.html. (accessed: 24.07.2024).

[29] G. M. Wysin. *Quantization of the Free Electromagnetic Field: Photons and Operators*. URL: http://www.phys.ksu.edu/personal/wysin. (accessed: 24.05.2024).

[30] LLC XIA. *Digital X-ray Processor User's Manual*. Version 1.0.x. Model DXP-XMAP. Hayward, CA 94544 USA.

[31] Roberto Zucchini. *Quantum Mechanics, Lecture Notes*. Dipartimento di Fisica ed Astronomia, Università di Bologna, I.N.F.N., sezione di Bologna. 2023.